1-1-2014

Simplified mapping rule for bounding surface simulation of complex loading paths in granular materials

Mojtaba E. Kan
University of New South Wales, mojtaba@uow.edu.au

Hossein Taiebat
University of New South Wales, h.taiebat@unsw.edu.au

Nasser Khalili
University of New South Wales, n.khalil@unsw.edu.au

Simplified mapping rule for bounding surface simulation of complex loading paths in granular materials

Abstract

This paper presents a bounding surface plasticity model that can be used to simulate complex monotonic and cyclic loading paths.A new mapping rule that only uses the last stress reversal point is introduced to describe the stress-strain behavior of granular soils during loading and unloading. This mapping rule is easy to implement and is suitable for highly erratic cyclic loading conditions, e.g., those induced by earthquake or traffic loading. The application and performance of the model are demonstrated using the results of experimental tests with various stress paths conducted under both monotonic and cyclic loading conditions. The study shows the efficiency of the new mapping rule in cap- turing the characteristic features of the behavior of granular soils under various loading paths.

Disciplines

Engineering | Science and Technology Studies

A Simplified Mapping Rule for Bounding Surface Simulation of Complex Loading Paths in Granular Materials

Mojtaba E. Kan[1]; Hossein A. Taiebat[2] and Nasser Khalili[3]

Abstract: This paper presents a bounding surface plasticity model that can be used to simulate complex monotonic and cyclic loading paths. A new mapping rule which only uses the last stress reversal point is introduced to describe the stress-strain behaviour of granular soils during loading and unloading. This mapping rule is easy to implement and is suitable for highly erratic cyclic loading condition, e.g. those induced by earthquake or traffic loading. The application and performance of the model is demonstrated using the results of experimental tests with various stress paths conducted under both monotonic and cyclic loading conditions. The study shows the efficiency of the new mapping rule in capturing the characteristic features of the behaviour of granular soils under various loading paths.

Keywords: bounding surface plasticity; mapping rule; cyclic loading; granular soil

[1] Research scholar, School of Civil and Environmental Engineering, The University of New South Wales, Sydney, NSW 2052, Australia. Email: m.esfahanikan@unsw.edu.au

[2] Senior Lecturer, School of Civil and Environmental Engineering, The University of New South Wales, Sydney, NSW 2052, Australia. Email: h.taiebat@unsw.edu.au

[3] Professor, School of Civil and Environmental Engineering, The University of New South Wales, Sydney, NSW 2052, Australia. Email: n.khalil@unsw.edu.au

INTRODUCTION

The concept of bounding surface plasticity was first introduced by Dafalias and Popov (1975) and Krieg (1975) to model nonlinear behaviour of materials under complex loading. In this approach, the plastic deformation at a stress point is calculated by defining the plastic modulus as a decreasing function of the distance of the stress point from its "image point" on a limiting surface called the bounding surface. This provides a smooth transition of stiffness from elastic to elastic-plastic state. By using a three-segmented bounding surface with a simple radial projection rule and a distance dependent additive plastic modulus, Dafalias and Hermann (1980) applied the theory of bounding surface plasticity to cohesive soils. Later, Bardet (1986) extended the application of the bounding surface models to nonlinear irreversible behaviour of sands, including strain softening and stress dilatancy observed in dense sands. This was achieved by defining the plastic modulus as a function of the mean effective stress and the stress ratio. However, the model proposed was based on the associativity of flow rule, and was unable to capture the post-peak strain-softening behaviour of loose sands under undrained shearing. Further developments of the bounding surface model were due to Crouch (1994) for 2D cases and Crouch and Wolf (1994a&b) for 3D cases, in which the combined radial and deviatoric mapping rules, non-associate flow rule, the bi-linear critical state line and the apparent normal consolidation line for sands were included. The shortcomings of this model were the complex shape of bounding surface, lack of continuity between the two mapping regions used in the model and the large number of model parameters.

More recently, a more rigorous bounding surface model based on the concept of the critical state soil mechanics was developed at The University of New South Wales (UNSW) by Russell and Khalili (2004) to model the stress-strain behaviour of sands. Later Khalili *et al.* (2005 & 2008) extended the model to simulate the behaviour of sands subjected to cyclic

43 loading under saturated and unsaturated states including hydraulic hysteresis effects. In this

44 model, hereafter referred to as UNSW constitutive model, the shape of the bounding surface

45 was obtained from experimental observations of undrained stress path responses of soils at

46 their loosest state. A mapping rule, passing through stress reversal points, was introduced to

47 predict the stress-strain behaviour under loading and unloading. Compared with the classical

48 bounding surface models, UNSW model was able to capture well the characteristic features of

49 granular soils subjected to cyclic loading (e.g. the contraction during deviatoric unloading), as

50 well as the behaviour of normally and over consolidated clayey materials. However, the

51 mapping rule adopted, despite its excellent performance in capturing the cyclic behavior of

52 soils, could not be applied efficiently to highly variable loading paths due to its complex

53 procedure and the storage and memory requirement in a boundary value problem. To tackle

54 this problem, a single stress point mapping rule is introduced in this study which has a simpler

55 procedure and is more amenable to application to complex loading paths. The performance of

56 the new mapping rule is illustrated by comparing the results of simulation of the model using

57 the two mapping rules. The new mapping rule is then employed to simulate the behaviour of

58 different soils under various monotonic and cyclic loading paths.

59 The novel aspects of the current work are threefold:

60   • The model formulation is extended to three-dimensional stress space (i.e. $p' - q - \theta$).

61   • A new mapping rule is introduced which has less complexity and brings more

62   robustness and efficiency in numerical modelling of highly complex cyclic loading

63   paths; e.g. earthquake loading.

64   • A host of new simulations, for a variety of different stress paths, including

65   conventional drained and undrained triaxial tests, constant mean effective stress tests,

66   constant confining stress tests, anisotropically consolidated and anisotropic

67   compression tests are presented to highlight the capabilities of the model. A single set

68   of parameters are used for each material in all simulations, though the experimental

69   data are taken from different references in the literature.

PRELIMINARIES

70

Notation

71

72 Soil mechanics sign is adopted throughout. Compression is taken as positive and tension as

73 negative. For the sake of simplicity, all derivations are presented in the $p' - q$ plane in a

74 three-dimensional stress space such that

$$p' = -\frac{I'}{3}, \; q = \sqrt{3J_2} \tag{1}$$

75

76 where $I' = \boldsymbol{\sigma}^T \boldsymbol{\delta}$ is the first invariant of the effective stress tensor, $J_2 = \frac{1}{2}\left(\mathbf{s}^T\mathbf{s}\right)$ is the second

77 invariant of the deviator stress tensor, $\mathbf{s} = \boldsymbol{\sigma} - \frac{1}{3}\left(\boldsymbol{\sigma}^T\boldsymbol{\delta}\right)\boldsymbol{\delta}$, and δ is Kronecker delta. The

78 corresponding strain conjugates are

$$\varepsilon_v = -\widehat{I}, \; \varepsilon_q = \frac{2}{\sqrt{3}}\sqrt{\widehat{J}_2} \tag{2}$$

79

80 where $\widehat{I} = \varepsilon^T \boldsymbol{\delta}$ and $\widehat{J}_2 = \frac{1}{2}\left(\widehat{\mathbf{s}}^T\widehat{\mathbf{s}}\right)$ are the first and the second invariants of the strain vector,

81 respectively, and $\widehat{\mathbf{s}} = \boldsymbol{\varepsilon} - \frac{1}{3}\left(\boldsymbol{\varepsilon}^T\boldsymbol{\delta}\right)\boldsymbol{\delta}$.

82 The total strain increments are divided into elastic and plastic components as

$$\dot{\varepsilon} = \dot{\varepsilon}^e + \dot{\varepsilon}^p \tag{3}$$

83

4

84   where the superscripts e and p denote the elastic and plastic components, respectively. The

85   volumetric strain, ε_v, is related to the specific volume (υ) as

86
$$\varepsilon_v = \ln(\frac{\upsilon}{\upsilon_0}) \tag{4}$$

87   where $\upsilon_0 = 1 + e_0$ is the specific volume at the reference mean effective stress, $\upsilon = 1 + e$, and e

88   and e_0 are the current void ratio and the void ratio at the reference point, respectively. The

89   material behaviour is assumed isotropic and rate independent.

Critical State

91   The critical state is the ultimate condition towards which all states approach with increasing

92   deviatoric shear strain. Figure 1 shows the Critical State Line (CSL) in the $\upsilon - \ln p'$ plane,

93   approximated by two linear segments (after Been *et al.*, 1991). More specifically, four

94   parameters are used to define the critical state line (CSL) in the $\upsilon - \ln p'$ plane: λ_0 and Γ_0 are

95   the slope of the initial portion of the CSL and its specific volume at $p' = 1kPa$, respectively;

96   p'_{cr} is the mean effective stress at the onset of particle crushing; and λ_{cr} is the slope of CSL

97   during the particle crushing stage. A dimensionless state parameter (ξ) is defined as a measure

98   of consistency of the soil under its current state; it is positive on the loose side of CSL and

99   negative on the dense side, and is defined as

100
$$\xi = \upsilon - \upsilon_{cs} \tag{5}$$

101   where υ is the specific volume at the current stress, p', and υ_{cs} is the specific volume at the

102   critical state corresponding to p'.

103   The CSL in the $q - p'$ plane is defined as a straight line passing through the origin. Following

104   Sheng *et al.* (2000), the slope of the CSL, M_{cs}, is defined as a function of Lode angle, θ,

$$M_{cs}(\theta) = M_{max}\left(\frac{2\alpha^4}{1+\alpha^4-(1-\alpha^4)\sin 3\theta}\right)^{\frac{1}{4}} \tag{6}$$

106   where θ is defined as $\theta = \frac{1}{3}\sin^{-1}\left(-\frac{3\sqrt{3}}{2}\frac{J_3}{\sqrt{(J_2)^3}}\right)$, J_2 and J_3 are the second and third

107   invariants of stress vector. Lode angle ranges from $\theta = -\frac{\pi}{6}$ for triaxial extension to $\theta = +\frac{\pi}{6}$

108   for triaxial compression. Here, α is a function of the strength parameter of soil and can be

109   given as

$$\alpha = \frac{3-\sin\varphi'_{cs}}{3+\sin\varphi'_{cs}} \tag{7}$$

111   where ϕ'_{cs} is the critical state internal frictional angle and is considered independent of

112   crushing of particles. M_{max} is the value of M_{cs} for triaxial compression which is linked to the

113   critical state friction angle and can be given as

$$M_{max} = \frac{6\sin\phi'_{cs}}{3-\sin\phi'_{cs}} \tag{8}$$

115   The proposed shape of the failure surface coincides with the Mohr-Coulomb failure surface at

116   all vertices in the deviatoric plane. It is also noted that $\alpha = 1$ recovers the von Mises failure

117   surface.

118   The Limiting Isotropic Compression Line (LICL) is defined as parallel to the CSL with a

119   constant shift in $\upsilon - \ln p'$ plane along the recompression line, as shown in Figure 1, Similar to

120   the critical state line, the LICL is a reference line in the $q - p'$ space, which can be viewed as

121   locus of the loosest possible state for a soil under a given mean effective stress. Given the

122   expression of CSL as

123
$$\upsilon = f(p') \tag{9}$$

124   the LICL is expressed as

125
$$\upsilon = f(\bar{p}') = f(p') - \kappa \ln R \tag{10}$$

126   where $\bar{p}' = R.p'$, and R is a model parameter.

127   **STRESS STRAIN RELATIONSHIP**

128   The incremental elastic strains are linked to the incremental stresses through

129
$$\dot{\boldsymbol{\sigma}}' = \mathbf{D}^e \dot{\boldsymbol{\varepsilon}}^e \tag{11}$$

130   where $\mathbf{D}^e$ is the elastic property matrix which can be defined as a function of the bulk

131   modulus, K, and the shear modulus, G.

132   The incremental plastic strain-stress relationship is written as

133
$$\dot{\boldsymbol{\varepsilon}}^p = \frac{1}{h} \mathbf{m} \mathbf{n}^T \dot{\boldsymbol{\sigma}}' \tag{12}$$

134   where $\mathbf{n}$ is the unit vector normal to the loading surface at the current stress state, $\boldsymbol{\sigma}'$, $\mathbf{m}$ is

135   the unit direction of plastic flow at $\boldsymbol{\sigma}'$, and h is the hardening modulus. Substituting (12) and

136   (3) in (11) the elastic-plastic stress-strain relationship is obtained as

137
$$\dot{\boldsymbol{\sigma}}' = \left(\mathbf{D}^e - \frac{\mathbf{D}^e \mathbf{m} \mathbf{n}^T \mathbf{D}^e}{h + \mathbf{n}^T \mathbf{D}^e \mathbf{m}} \right) \dot{\boldsymbol{\varepsilon}} \tag{13}$$

138 The bulk and shear elastic moduli are calculated assuming that unloading/reloading occurs

139 along a κ line in the $\upsilon - \ln p'$ plane. The moduli are then defined as

$$K = \frac{\upsilon p'}{\kappa} \qquad (14)$$

141

$$G = \frac{3(1-2v)}{2(1+v)} \frac{\upsilon p'}{\kappa} \qquad (15)$$

142 where v is the Poisson's ratio.

ELASTO-PLASTIC BEHAVIOUR

144 The essential elements of a bounding surface plasticity model are: (i) a bounding surface for

145 describing the limit states of stress; (ii) a loading surface on which the current stress state lies

146 and a mapping rule to find the image point on the bounding surface; (iii) a plastic potential for

147 describing the mode and magnitudes of plastic deformations, and (iv) a hardening rule for

148 controlling the size of the bounding surface and the location of the loading surfaces.

149 Following the work of Khalili *et al.* (2005), the domain of purely elastic response is assumed

150 to be nil and all deformation is considered elastic-plastic. This is achieved by defining the

151 hardening modulus, *h*, as a decreasing function of the distance between the stress state, $\boldsymbol{\sigma'}$, and

152 an "image point", $\bar{\boldsymbol{\sigma}}'$ on the bounding surface. During loading the size of the loading surface

153 increases so that any unloading/reloading results in elastic-plastic deformation. Detailed

154 definitions of the bounding surface, the loading surface and mapping rule, the plastic potential,

155 and the hardening rule are given in the following sections. The stress conditions on the

156 bounding surface are denoted using a superimposed bar throughout this notes.

Bounding Surface

158   Accurate descriptions of the bounding surface are required in order to avoid complications in

159   the stress-strain simulations of soil, particularly under undrained conditions. The shape of the

160   bounding surface is best selected experimentally. It can be determined from the undrained

161   response of the material at its loosest state. It should be mentioned that the undrained response

162   of the material in the effective stress space follows the bounding surface when the

163   contribution of elasticity to volume change is negligible. Examining a host of experimental

164   data, Russell and Khalili (2004) and Khalili *et al.* (2005) suggested the following expression

165   for the shape of the bounding surface:

166
$$F\left(\bar{p}',\bar{q},\bar{\theta},\bar{p}'_c\right)=\left(\frac{\bar{q}}{M_{cs}\left(\bar{\theta}\right)\bar{p}'}\right)^{N}-\frac{\ln\left(\bar{p}'_c/\bar{p}'\right)}{\ln R}=0 \tag{16}$$

167   The parameter $\bar{p}'_c$ controls the size of the bounding surface and is a function of the plastic

168   volumetric strain. The material constant R represents the ratio of $\bar{p}'_c$ and the mean effective

169   stress at the intercept of the bounding surface with the CSL in the $q-p'$ space. The constant

170   N controls the curvature of the bounding surface. The effects of different magnitudes of N

171   and R on the three-dimensional shape of the bounding surface are illustrated in Figure 2.

172   **Loading Surface and Mapping Rule**

173   The loading surface is assumed to be of the same shape as the bounding surface. For first time

174   loading these two surfaces are homologous about the origin of the stress coordinate system. In

175   this case, the function for the loading surface takes the form of

176
$$F\left(p',q,\theta,p'_c\right)=\left(\frac{q}{M_{cs}\left(\theta\right)p'}\right)^{N}-\frac{\ln\left(p'_c/p'\right)}{\ln R}=0 \tag{17}$$

177   where p'_c is the isotropic hardening parameter controlling the size of the loading surface as

178   illustrated in Figure 3. The state of stress, $\boldsymbol{\sigma}'$, is always located on the loading surface. An

179   image for the state of stress can be found on the bounding surface, $\bar{\boldsymbol{\sigma}}'$, as shown in Figure 3.

180   The centre of homology, $\boldsymbol{\sigma}'$ and $\bar{\boldsymbol{\sigma}}'$ are used to define the mapping rule. For unloading and

181   reloading conditions, the centre of homology moves to the last point of stress reversal.   The

182   point of stress reversal is identified when the product of the normal vector to the bounding

183   surface $(\mathbf{n})$ and the vector of the stress increment $(\dot{\boldsymbol{\sigma}}'_e)$ becomes negative (Pastor *et al,* 1990),

184   where $\dot{\boldsymbol{\sigma}}'_e$ is calculated using the total strain as $\mathbf{D}^e \times \dot{\boldsymbol{\varepsilon}}$. The image of the stress point in the

185   $p' - q$ plane is located using the Pegasus method (Dowell and Jarratt, 1972 and Sloan *et al.*,

186   2001).   Upon stress reversal, a new loading surface is formed with the new centre of

187   homology, as shown in Figure 4a. To maintain similarity with the bounding surface, the

188   loading surfaces undergo kinematic hardening during loading and unloading. This mapping

189   rule is simpler and easier to be implemented as compared to the one used originally by Khalili

190   *et al.* (2005).

191   In order to locate the image point for unloading/reloading condition, Khalili *et al.* (2005)

192   introduced the maximum loading surface at the point of stress reversal as the local bounding

193   surface and formed a new loading surface at the centre of homology. The image point was

194   then located sequentially by projecting the stress point onto a series of intermediate image

195   points on successive local bounding surfaces each passing through a point of stress reversal

196   (Figure 4b). The loading history of the soil was captured through the stress reversal points and

197   the corresponding maximum loading surfaces. Application of such a complex mapping rule is

198   not efficient in simulation of a boundary value problem with highly erratic cyclic loading

199   paths, such as those that occur under earthquake loading conditions. The history of stress

200   reversal points and the geometry of intermediate local bounding surfaces should also be

201 tracked during unloading/reloading conditions, which increases the memory requirement in a

202 large boundary value problem.

203 The new single stress point mapping rule, proposed in this study, locates the image point

204 directly on the bounding surface, as shown in Figure 4a, without forming successive

205 intermediate local bounding surfaces. This version of the mapping rule is easier to be

206 implemented, does not require the history of previous loading surfaces, and is more suitable

207 for simulation of high frequency cyclic loading, e.g. due to earthquake, vibration, traffic

208 loading and blasting and real life applications where previous stress history of the soil is

209 unknown.

210 The unit normal vector at the image point defining the direction of loading is given using the

211 general equation:

212
$$\mathbf{n} = \frac{\partial F / \partial \overline{\mathbf{\sigma}}'}{\left\| \partial F / \partial \overline{\mathbf{\sigma}}' \right\|} \tag{18}$$

213 The vector $\partial F / \partial \overline{\mathbf{\sigma}}'$ is evaluated applying the chain rule of differentiation:

214
$$\frac{\partial F}{\partial \overline{\sigma}'} = \frac{\partial F}{\partial \overline{p}'} \frac{\partial \overline{p}'}{\partial \overline{\sigma}'} + \frac{\partial F}{\partial \overline{q}'} \frac{\partial \overline{q}'}{\partial \overline{\sigma}'} + \frac{\partial F}{\partial \overline{\theta}'} \frac{\partial \overline{\theta}'}{\partial \overline{\sigma}'} \tag{19}$$

215 Recalling the generalized definitions of the invariants $\overline{p}', \overline{q}$ and $\overline{\theta}$, their derivatives with

216 respect to $\overline{\mathbf{\sigma}}'$ become

217
$$\frac{\partial \overline{p}'}{\partial \overline{\mathbf{\sigma}}'} = -\frac{1}{3} \mathbf{\delta} \tag{20}$$

218
$$\frac{\partial \overline{q}'}{\partial \overline{\mathbf{\sigma}}'} = \frac{3}{2\overline{q}} \left(\overline{\mathbf{\sigma}}' - \mathbf{\delta} \frac{\overline{I}}{3} \right) \tag{21}$$

219

$$\frac{\partial \bar{\theta}}{\partial \boldsymbol{\sigma}'} = -\frac{\sqrt{3}}{2\sqrt{\bar{J}_2^3}\cos 3\bar{\theta}} \left(\frac{\partial \bar{J}_3}{\partial \boldsymbol{\sigma}'} - \frac{3\bar{J}_3}{2\bar{J}_2} \frac{\partial \bar{J}_2}{\partial \boldsymbol{\sigma}'} \right)$$

(22)

220    $\partial F/\partial \bar{p}'$, $\partial F/\partial \bar{q}$ and $\partial F/\partial \bar{\theta}$ are evaluated by differentiating the generalized form of equation

221   (16) with respect to $\bar{p}'$, $\bar{q}$ and $\bar{\theta}$

222

$$\frac{\partial F}{\partial \bar{p}'} = -\frac{N}{\bar{p}'} \left(\frac{\bar{q}}{M_{cs}(\bar{\theta})\bar{p}'} \right)^N + \frac{1}{\bar{p}' \ln R}$$

(23)

223

$$\frac{\partial F}{\partial \bar{q}} = \frac{N}{M_{cs}(\bar{\theta})\bar{p}'} \left(\frac{\bar{q}}{M_{cs}(\bar{\theta})\bar{p}'} \right)^{N-1} = \frac{N}{\bar{q}} \left(\frac{\bar{q}}{M_{cs}(\bar{\theta})\bar{p}'} \right)^N$$

(24)

224

$$\frac{\partial F}{\partial \bar{\theta}} = -\frac{3N}{4} \left(\frac{\bar{q}}{M_{cs}(\bar{\theta})\bar{p}'} \right)^N \left(\frac{(1-\alpha^4)\cos 3\bar{\theta}}{1+\alpha^4-(1-\alpha^4)\sin 3\bar{\theta}} \right)$$

(25)

225   **Plastic Potential**

226   The plastic potential defines the direction of plastic strain increments. Since plastic behaviour

227   is characterized by the link between strain increments and stresses, the plastic potential is

228   generally expressed using a plastic flow rule relating the plastic dilatancy ($d = \dot{\varepsilon}_v^p / \dot{\varepsilon}_q^p$) to the

229   stress ratio q/p'. In this work, the plastic potential (g) is defined as

230

$$g(p', q, \bar{\theta}, p_o) = \tilde{t}q + \frac{AM_{cs}(\bar{\theta})p'}{A-1} \left(\left(\frac{p'}{p_o} \right)^{A-1} - 1 \right) \quad \text{for } A \neq 1$$

(26)

231

$$g(p', q, \bar{\theta}, p_o) = \tilde{t}q + M_{cs}(\bar{\theta})p' \ln \left(\frac{p'}{p_o} \right) \quad \text{for } A = 1$$

(27)

232   where p_0 controls the size of the plastic potential, though it is not required in the model since

233   only derivatives of the (g) function are incorporated in formulations, and A is a material

234   parameter. The direction of plastic flow is defined by:

$$\mathbf{m} = \frac{\partial g / \partial \boldsymbol{\sigma}'}{\left\| \partial g / \partial \boldsymbol{\sigma}' \right\|} \tag{28}$$

235

236   in which $\partial g / \partial \boldsymbol{\sigma}'$ is evaluated applying the chain rule of differentiation:

$$\frac{\partial g}{\partial \boldsymbol{\sigma}'} = \frac{\partial g}{\partial p'} \frac{\partial p'}{\partial \boldsymbol{\sigma}'} + \frac{\partial g}{\partial q} \frac{\partial q}{\partial \boldsymbol{\sigma}'} + \frac{\partial g}{\partial \bar{\theta}} \frac{\partial \bar{\theta}}{\partial \boldsymbol{\sigma}'} \tag{29}$$

237

238    $\partial g / \partial p'$, $\partial g / \partial q$ and $\partial g / \partial \theta$ are evaluated by differentiating the plastic potential with respect

239   to p', q and $\bar{\theta}$.

$$\frac{\partial g}{\partial p'} = A \left(M_{cs} \left(\bar{\theta} \right) - \tilde{t} \frac{q}{p'} \right) \tag{30}$$

240

$$\frac{\partial g}{\partial q} = \tilde{t} \tag{31}$$

241

$$\frac{\partial g}{\partial \bar{\theta}} = -\tilde{t} \frac{3q}{4} \left(\frac{(1 - \alpha^4) \cos 3\bar{\theta}}{1 + \alpha^4 - (1 - \alpha^4) \sin 3\bar{\theta}} \right) \tag{32}$$

242

243   In the above equations $\tilde{t}$ is a scalar, the sign of which controls the direction of plastic flow in

244   the deviatoric plane. At any stress point two vectors of plastic flow are identified, one

245   corresponding to compressive loading (m^+) and the other to extensive (m^-) as shown in

246   Figure 5. The direction of plastic flow is controlled by $\tilde{t}$, which is determined based on the

247   relative positions of the stress point, $\boldsymbol{\sigma}'$, and its image point, $\bar{\boldsymbol{\sigma}}'$, by comparing the angle

248   between a given reference axis and the stress point (γ_σ) and the angle between the reference

249   axis and the image point $(\gamma_{\bar{\sigma}})$:

$$\tilde{t} = +1 \qquad \text{for } |\gamma_{\bar{\sigma}} - \gamma_\sigma| < \pi / 2 \tag{33}$$

$$\tilde{t} = -1 \qquad \text{for } |\gamma_{\bar{\sigma}} - \gamma_\sigma| > \pi / 2 \tag{34}$$

Hardening Modulus

253   In the bounding surface plasticity, the hardening modulus h consist of two components

$$h = h_b + h_f \tag{35}$$

255   where h_b is the plastic modulus at $\bar{\sigma}'$ on the bounding surface, and h_f is plastic modulus at

256   σ' and defined as a function of the distance between σ' and $\bar{\sigma}'$. Applying the consistency

257   condition at the bounding surface and assuming isotropic hardening of the bounding surface

258   with plastic volumetric compression, the derivative of the bounding surface can be obtained

259   as

$$\dot{F} = \left(\frac{\partial F}{\partial \boldsymbol{\sigma}'} \right)^T \dot{\boldsymbol{\sigma}}' + \frac{\partial F}{\partial \overline{p}_c'} \frac{\partial \overline{p}_c'}{\partial \varepsilon_v^p} \dot{\varepsilon}_v^p \tag{36}$$

261   Then, the flow rule will be

$$\dot{\varepsilon}_v^p = \dot{\Lambda} \frac{\partial g}{\partial p'} \tag{37}$$

263   Using the definition of the unit vector normal to the bounding surface, equation (37) can be

264   rewritten as

$$\dot{F} = \mathbf{n}^T \dot{\boldsymbol{\sigma}}' - \dot{\Lambda} h_b = 0 \tag{38}$$

266   in which h_b is calculated as

$$h_b = -\frac{\partial F}{\partial \bar{p}'_c} \frac{\partial \bar{p}'_c}{\partial \varepsilon_v^p} \frac{m_p}{\left\| \partial F / \partial \bar{\boldsymbol{\sigma}}' \right\|} \tag{39}$$

268   with $m_p = \dfrac{\partial g / \partial \bar{p}'}{\left\| \partial g / \partial \boldsymbol{\sigma}' \right\|}$. Differentiating equation (16) with respect to $\bar{p}'_c$ yields to

$$\frac{\partial F}{\partial \bar{p}'_c} = \frac{-1}{\bar{p}'_c \ln R} \tag{40}$$

270   For isotropic hardening rule, the evolution of $\bar{p}'_c$ with ε_v^p is in turn given by

$$\frac{\partial \bar{p}'_c}{\partial \varepsilon_v^p} = \frac{\upsilon \bar{p}'_c}{\lambda - \kappa} \tag{41}$$

272   where λ is the current slope of the LICL in the $\upsilon - \ln p'$. Substituting equations (40) and (41)

273   into equation (39) yields

$$h_b = \frac{\upsilon}{(\lambda - \kappa) \ln R} \frac{m_p}{\left\| \partial F / \partial \bar{\boldsymbol{\sigma}}' \right\|} \tag{42}$$

275   The modulus h_f is defined such that it is zero on the bounding surface and infinity at the point

276   of stress reversal, and can take from of

$$h_f = \frac{\upsilon p'}{(\lambda - \kappa)} \left(\frac{\bar{p}'_c}{p'_c} - 1 \right) k_m \left(\eta_p - \tilde{t} \eta \right) \tag{43}$$

278   where $\bar{p}_c{'}$ and p'_c define the sizes of the bounding and loading surfaces, respectively, η_p is

279   the slope of the peak strength line in the $q - p'$ plane, and k_m is a scaling parameter

280   controlling the steepness of the response in the $q - \varepsilon_q$ plane. The slope of the peak strength

15

line is a function of the state parameter and the slope of the critical state line, which is given as

$$\eta_p = \tilde{t}\left(1 - k\xi\right)M_{cs} \tag{44}$$

where k is a material parameter.

The scaling parameter k_m can be taken as a material constant for some soils, though it is strongly influenced by the initial state parameters and the loading direction (Khalili *et al.*, 2005). Russell and Khalili (2004&2006), examined a wide range of triaxial tests on granular materials and concluded that k_m can be expressed as a function of the initial value of the dimensionless state parameter, ξ_0 (equation 5) and initial confining pressure, p_0'. In this study a general expression for k_m is suggested as follows:

$$k_m = k_{m0}\langle 1.0 - \beta_1\exp(\xi_0)\rangle(p_0')^{\beta_2} \tag{45}$$

where k_{m0}, β_1 and β_2 are material parameters.

APPLICATION

To demonstrate robustness and application of the model, a series of comparative simulations is first performed using the new and the original mapping rules (Khalili *et al.*, 2005). This is followed by a host of non-standard monotonic and complex cyclic simulations.

Performance of the New Mapping Rule

To examine the effect of the mapping rule on the performance of the model, cyclic responses of Hostun, Fuji River and Toyoura sands are investigated.

300   The results of the drained cyclic test simulation on a dense sample of Hostun sand using the

301   original mapping rule (Khalili *at al*. (2005) and the simplified one are presented in Figure 6.

302   Also shown in this figure are the experimental data reported by Saada *et al*. (1989). The initial

303   conditions of the sample were $p' = 350kPa$ and $\upsilon = 1.61$ and the material parameters are

304   selected as $\kappa = 0.003$, $\nu = 0.1$, $M_{cs} = 1.31$, $\lambda_0 = 0.028$, $\lambda_{cr} = 0.24$, $\Gamma_0 = 2.037$, $N = 2.3$,

305    $R = 7.5$, $A = 1.0$ and $k = 2.0$ with $k_m = 3.5$ for the first time loading and $k_m = 35.0$ for

306   unloading and reloading, similar to those used by Khalili *et al*. (2005).

307   Figure 6 shows that the performance of the new mapping rule is as good as that of the more

308   complex original mapping rule when compared with the results of the experimental data. Both

309   mapping rules capture the stiffening of the material response during unloading and reloading,

310   simulate the contraction of the sample during unloading and the subsequent dilation during

311   reloading. A better match with the experimental data could have been achieved if the model

312   properties were calibrated for the new mapping rule however this was avoided for the sake of

313   consistency of the comparisons.

314   Figure 7 shows the results of simulation of a cyclic drained test on loose Fuji River sand

315   conducted by Tatsuoka and Ishihara (1974), where the variations of stress ratio versus

316   deviatoric and volumetric strains are presented. In this test the amplitude of the cyclic loading

317   increases gradually at each cycle. The initial conditions of the sample were $p' = 196kPa$ and

318    $\upsilon = 1.74$. The basic material parameters are selected according to those used by Khalili *et al*.

319   (2005), i.e., $\kappa = 0.01$, $\nu = 0.3$, $M_{cs} = 1.48$, $\lambda_0 = 0.032$, $\lambda_{cr} = 0.21$, $\Gamma_0 = 1.870$, $N = 3.0$,

320    $R = 6.2$, $A = 1.0$ and $k = 2.0$; with $k_m = 0.13$ for the first time loading and $k_m = 8.0$ for

321   unloading and reloading.

322   The results of the simulations show that both mapping rules capture the main features of the

323   behavior of the sand under cyclic loading. The predictions of the two mapping rules are very

17

324   similar, except that the new mapping rule predicts a larger volumetric strain than the original

325   mapping rule. However, when compared with the experimental data, the performance of the

326   new mapping rule can be regarded to be as good as the original mapping rule. Figure 7 shows

327   that simplifications of the original mapping rule do not affect the performance of the model,

328   in particular, in simulation of the contractive responses during loading and unloading and the

329   stiffening of the behaviour with successive cycles.

330   The effects of the two mapping rules on the response of the model are also shown in Figure 8,

331   where the results of simulation for a drained cyclic test on Toyoura sand with constant mean

332   effective stress (Pradhan *et al.* 1989b) are presented. The material parameters and state

333   variables are taken to be the same in both simulations, i.e., $p' = 98.1 kPa$, $\upsilon = 1.845$

334    $\kappa = 0.001$, $v = 0.3$, $M_{cs} = 1.24$, $\lambda_0 = 0.03$, $\lambda_{cr} = 0.24$, $\Gamma_0 = 1.969$, $N = 3.0$, $R = 5.8$,

335    $A = 1.0$, $k = 2.0$; with $k_m = 1.0$ for the first time loading and $k_m = 3.0$ for unloading and

336   reloading. Once again both simulations result in very close match with the experimental data.

337   Figure 8 shows noticeable differences in the volumetric strains predicted by the two mapping

338   rules, especially under low cyclic load amplitudes; the volumetric strain is overestimated by

339   the original mapping rule and underestimated by the new mapping rule, when compared with

340   the experimental data. However, under higher cyclic amplitude the performance of the model

341   with the new mapping rule is superior to that with the original mapping rule.

342   A comparison of the results of the simulations of the model using the two mapping rules

343   indicates that the simplification of the original mapping rule does not affect the performance

344   of the model, especially when the results are compared with the experimental data. The new

345   mapping rule has the advantages of being robust and simpler than the original one and

346   therefore is recommended to be used for complex cyclic loading.

Further Validation

To further examine the performance of the model with the new mapping rule a number of well documented cases from literature are selected and analyzed, such as tests on Nevada sand (Arulmoli et al., 1992) and Toyoura sand (Verdugo and Ishihara, 1996, and Pradhan *et al.,* 1989a). The material parameters used for these simulations are listed in Table 1 and Table 2. The procedure to obtain the material parameters are described by Russell and Khalili (2004) and Khalili *et al.* (2005).

Drained and Undrained Tests on Nevada Sand

Nevada sand was used in VELACS project (Arulmoli *et al.*, 1992) under both 1g laboratory conditions and in centrifuge experiments. The triaxial experiments reported in that project are used here for calibration purpose as well as for verification of the performance of the model. Kutter *et al.* (1994) and Chen (1995) have also reported the results of a series of triaxial and torsional shear tests on Nevada sand which are used in this study for definition of the material properties. Samples of the triaxial tests in VELACS project were 63.5*mm* in diameter and prepared using dry pluviation method. The samples were subjected to a variety of non-standard drained and undrained monotonic stress paths, among them are those of triaxial compression tests shown in Figure 9. The triaxial experiments were performed on both loose $(D_r = 40\%)$ and dense $(D_r = 60\%)$ samples under different confining pressures. The material parameters are shown in Table 1and Table 2.

The results of the simulation of CIDC tests (Figure 9) on loose as well as dense samples of Nevada sand are presented in Figure 10 and Figure 11, respectively. These tests were conducted under drained conditions where the samples were loaded isotropically under 3 different confining pressures of $p'_0 = 40, 80, 160 kPa$, followed by loading under constant mean effective stresses. The model captures the experimentally observed initial hardening

19

371   behaviour of loose sands accompanied by a volumetric contraction until the critical state is

372   reached (Figure 10). For the dense sand the experimental data do not show a clear softening

373   due the fact that the tests were conducted under constant mean effective stress and the model

374   captures such a behaviour (Figure 11). Overall the prediction of the model is in strong

375   agreement with the test data.

376   The results of the simulation of CIUC tests (Figure 9) are presented in Figure 12 and Figure

377   13, for loose and dense samples, respectively. These tests were conducted in undrained

378   conditions under 3 different confining pressures. The model predicts stiffer response initially,

379   but the overall response matches the experimental data very well, especially in $q - p'$ plane.

380   Figure 14 and Figure 15 show the results of simulation of CADC tests under drained

381   conditions, during which samples of sand were first loaded isotropically to p'_0, followed by a

382   loading under constant mean effective stress, followed by a standard triaxial loading to a

383   mean effective stress of p'_1. The samples were then loaded to failure under constant mean

384   effective stress and under constant deviatoric stress, as shown in Figure 9 by $OO_1A_1A_2C_2$ and

385    $OO_1A_1A_2C_4$ stress paths, respectively. The tests were performed at relative densities of

386    $D_r = 40\%$ and 60%. In both cases the model simulates the experimental behaviour very well.

387   The main features of the response, including the peak strength in $q - \varepsilon_1$ plane as well as the

388   initial contraction followed by the progressive dilation in $\varepsilon_v - \varepsilon_1$ plane were captured by the

389   model. It is worth to mention that in CADC tests stress reversal occurs at point A_2 (refer to

390   Figure 9).

391   ***Drained and Undrained Tests on Toyoura Sand***

392   Toyoura sand has been used extensively by scholars for verification of different constitutive

393   models (e.g. Khalili *et al.*, 2005, Ling and Yang, 2006). In this study the experimental data on

394   Toyoura sand reported by Verdugo and Ishihara (1996) are used to verify the performance of

395   the UNSW model. The material parameters obtained by calibration of the model with these

396   tests are also used later to evaluate the performance of the model in simulating a different

397   series of tests reported by Pradhan *et al.* (1989a). The material parameters used for simulation

398   of these tests are shown in Table 1and Table 2.

399   Verdugo and Ishihara (1996) performed a series of drained and undrained monotonic triaxial

400   tests on Toyoura sand. The specimens were prepared using moist placement method. In the

401   drained tests, two different confining pressures of 100 and $500kPa$ were used for specimens

402   with three different void ratios, ranging from 0.81 to 0.996. The undrained tests were

403   conducted under a wider range of confining pressures, from 100 to 3000 kPa with different

404   void ratios corresponding to relative densities of $D_r = 16\%$ to 64%, corresponding to

405   consistencies from very loose to dense states for the soil under practical stress levels.

406   The results of the simulations of drained tests under $p_0' = 100kPa$ and $500kPa$ are shown in

407   Figure 16 and compared with experimental data. While there is a slight discrepancy between

408   the predicted performance and experimental data for the loose sample under the low confining

409   pressure, i.e. in test 3, the model predictions for other samples are in excellent agreement with

410   the observed data.

411   The performance and capability of the model to simulate the undrained behaviour of sands on

412   a wide range of initial conditions, including different relative densities and mean effective

413   stresses, are investigated using 7 undrained tests reported by Verdugo and Ishihara (1996).

414   The outcomes of these simulations are compared with the experimental data in Figure 17 for

415   mean effective stresses vary from 100 to 3000 kPa . In general, the comparison shows

416   satisfactory results, considering the fact that a single set of parameters is used for all

417   simulations under a large range of confining pressures.

418   The parameters calibrated from the experiments of Verdugo and Ishihara (1996) are also used

419   to simulate the drained behaviour of Toyoura sand reported by Pradhan *et al.* (1989a). The

420   experiments were conducted under various stress paths, including tests to failure under

421   constant axial stress, constant mean effective stress and constant radial pressure, as well as

422   conventional triaxial test (CTC) as shown in Figure 18

423   Figure 19 compares the results of simulations with the experimental data. The model captures

424   all features of the soil behaviour for different stress paths, with some minor discrepancies

425   where maximum large stress ratio is approached. This may be due to the fact that the Toyoura

426   sand used by Pradhan *et al.* (1989a) was of a different batch from Verdugo and Ishihara

427   (1996), and therefore requires slightly different parameters.

428

429   ***Cyclic Drained tests on Toyoura sand***

430   Pradhan *et al.* (1989b) performed a series of drained triaxial cyclic tests on Toyoura sand.

431   Four cyclic drained tests with constant mean effective stress are selected and used in this

432   study. To highlight the robustness of the proposed model, the material parameters obtained

433   from model calibration with the experimental tests conducted by Verdugo and Ishihara (1996)

434   are used in these simulations. The state parameters and initial conditions of the samples are

435   presented inTable 3.

436   Figure 20 and Figure 21 show results of drained cyclic tests conducted under constant mean

437   effective stresses on loose and dense samples of Toyoura sand. In these tests the amplitude of

438   the shear strain increases during cyclic loading. These figures show that the model can

439   simulate well the stress-strain response and the successive stiffening or softening of the

440   samples with cyclic loading. The results of the simulation under higher stress levels match

441   better with the experimental data. This may be due the fact that the model parameters are

442   obtained based on tests conducted on a range of stress levels, mostly greater than $1000kPa$,

443   which are greater than those used in Pradhan *et al.* (1989b) experimental tests, which are all

444   under $100kPa$.

445   Figure 22 shows the results of simulation of a drained cyclic test with a constant mean

446   effective stress on a very loose sample of Toyoura sand. In this test the amplitude of the shear

447   strain decreases during cyclic loading. This figure also shows the results of a simulation

448   performed by Ling and Yang (2006). The UNSW model captures the general behaviour

449   observed in the experiment, especially in the $\eta - \varepsilon_q$ plane. In $\varepsilon_v - \varepsilon_q$ plane the simulation

450   shows a lower volume change in the median cycles compared to the experimental data. Figure

451   22 shows the superior performance of the model over that presented by Ling and Yang (2006).

452   Figure 23 represents the results of simulation of a drained cyclic test on a very loose sample

453   of Toyoura sand under a constant mean effective stress and small hysteresis loops of

454   unloading and reloading. Once again, the model predicts the main features of the behaviour,

455   both in $\eta - \varepsilon_q$ plane and $\varepsilon_v - \varepsilon_q$ plane. It is worth mentioning that a better match between the

456   results of simulation and the test data could have been achieved if the model parameters were

457   calibrated for the same test rather than taking from those calibrated for tests performed by

458   Verdugo and Ishihara (1996).

459   ***Cyclic Undrained tests on Fuji River sand***

460   Ishihara *et al.* (1975) conducted a series of undrained triaxial cyclic tests on loose samples of

461   Fuji River sand to study the liquefaction phenomena. Loose samples were obtained by

462   spooning freshly boiled sand into the mold filled with de-aired water. Two of these tests are

463   selected for simulation to show the performance of UNSW model in capturing the undrained

464   behaviour of granular materials. The material parameters and the initial conditions of the

465   samples are listed in Table 1 and

466   Table 3, respectively. A constant value of k_m is used in these simulations due to the narrow

467   range of initial state parameters, as shown in Table 2.

468   Figure 24 presents the results of the undrained test conducted on loose Fuji River sand under a

469   cyclic loading with constant stress amplitude. Figure 25 shows the results for a test under

470   irregular cyclic stress amplitude. In both simulations the predicted behaviour is in good

471   agreement with the observed experimental data. The model captures the failure of the samples

472   by liquefaction in which the effective normal stress decreases progressively until the stress

473   path reaches the critical state and the material becomes unstable.

CONCLUSION

475   The UNSW bounding surface plasticity model has been proved to be a versatile constitutive

476   model capable of simulating the behaviour of sands over a wide range of stresses under

477   drained/undrained and monotonic/cyclic loading conditions. A relatively complex mapping

478   rule was initially formulated for the model which makes application of the model to

479   simulation of highly variable cyclic loading inefficient. In this study, a new mapping rule is

480   formulated which is less complex and more efficient for simulation of complex monotonic

481   and cyclic loadings of granular soils. The new mapping rule does not require a record of

482   history of successive intermediate local bounding surfaces, as was required in the original

483   mapping rule. Comparison of the results of simulations of the model using the original and the

484   new mapping rules indicated that the simplification incorporated in the new mapping rule

485   does not compromise the performance of the model. The robustness of the UNSW model with

486   the new mapping rule was demonstrated through simulations of static and cyclic loading

487   under drained and undrained conditions for different soils. The results of simulations were

488   invariably in excellent agreement with experimental data. The model captures the

489   characteristic features of the behaviour of different sands for a wide range of densities and

490   stresses, including the stress softening and dilatancy during drained loading of dense sands,

491   liquefaction of loose sands under undrained loading conditions, and the progressive stiffening

492   as well as hysteresis in the stress-strain relationships for cyclic loading. The versatility of the

493   model in simulation of particular sand was demonstrated using one set of material parameters

494   for all tests conducted on the sand under different conditions and by different investigators.

Acknowledgements

References

500   Arulmoli, K., Muraleetharan, K., Hossain, M., & Fruth, L. (1992). VELACS: Verification of

501   liquefaction analyses by centrifuge studies, laboratory testing program, soil data report.

502   *Research Report, The earth Technology Corporation.*

503   Bardet, J. (1986). Bounding surface plasticity model for sands. *Journal of Engineering*

504   *Mechanics, 112*(11), 1198-1217.

505   Been, K., Jefferies, M., & Hachey, J. (1991). The critical state of sands. *Geotechnique, 41*(3),

506   365-381.

507   Chen, Y. R. (1995). *Behavior of a fine sand in triaxial, torsional and rotational shear tests.*

508   PhD thesis, University of California, Davis.

509   Crouch, R. S. (1994). Unified Critical State Bounding Surface Plasticity Model for Soil.

510   *Journal of Engineering Mechanics, 120*(11), 2251-2270.

511   Crouch, R. S., & Wolf, J. P. (1994a). Unified 3D critical state bounding surface plasticity

512   model for soils incorporating continuous plastic loading under cyclic paths. Part II:

513   Calibration and simulations. *International Journal for Numerical and Analytical*

514   *Methods in Geomechanics, 18*(11), 759-784.

515   Crouch, R., & Wolf, J. (1994b). Unified 3D critical state bounding-surface plasticity model

516   for soils incorporating continuous plastic loading under cyclic paths. Part I: constitutive

517   relations. *International Journal for Numerical and Analytical Methods in*

518   *Geomechanics, 18*(11), 735-758.

519   Dafalias, Y., & Popov, E. (1975). A model of nonlinearly hardening materials for complex

520   loading. *Acta Mechanica, 21*(3), 173-192.

521   Dafalias, Y. F., & Herrmann, L. R. (1980). A bounding surface soil plasticity model.

522   *International Symposium on Soils under Cyclic and Transient Loading*, Swansea.

523   Dowell, M., & Jarratt, P. (1972). The "Pegasus" method for computing the root of an

524   equation. *BIT Numerical Mathematics, 12*(4), 503-508.

525   Ishihara, K., Tatsuoka, F., & Yasuda, S. (1975). Undrained deformation and liquefaction of

526   sand under cyclic stresses. *Soils and Foundations, 15*(1), 29-44.

527   Khalili, N., Habte, M., & Valliappan, S. (2005). A bounding surface plasticity model for

528   cyclic loading of granular soils. *International journal for numerical methods in*

529   *engineering, 63*(14), 1939-1960.

530   Khalili, N., Habte, M., & Zargarbashi, S. (2008). A fully coupled flow deformation model

531   for cyclic analysis of unsaturated soils including hydraulic and mechanical hystereses.

532   *Computers and Geotechnics, 35*(6), 872-889.

533   Krieg, R. (1975). A practical two surface plasticity theory. *Journal of applied mechanics,*

534   *ASME, 42*, 641.

535   Kutter, B. L., Chen, Y. R., & Shen, C. (1994). Triaxial and torsional shear test results for

536   sand, *Contract Report CR 94.003-SHR, Naval Facilities Engineering Service Center*.

537   Port Hueneme, CA 93043-4328.

538   Ling, H. I., & Yang, S. (2006). Unified sand model based on the critical state and

539   generalized plasticity. *Journal of Engineering Mechanics, 132*(12), 1380-1391.

540   Pastor, M., Zienkiewicz, O., & Chan, A. (1990). Generalized plasticity and the modelling of

541   soil behaviour. *International Journal for Numerical and Analytical Methods in*

542   *Geomechanics, 14*(3), 151-190.

543   Pradhan, T., Tatsuoka, F., Mohri, Y., & Sato, Y. (1989a). An atomated triaxial testing

544   system using a simple triaxial cell for soils. *Soils and Foundations, 29*(1), 151-160.

545   Pradhan, T., Tatsuoka, F., & Sato, Y. (1989b). Experimental stress-dilatancy relations of

546   sand subjected to cyclic loading. *Soils and Foundations, 29*(1), 45-64.

547   Russell, A. R., & Khalili, N. (2004). A bounding surface plasticity model for sands

548   exhibiting particle crushing. *Canadian Geotechnical Journal, 41*(6), 1179-1192.

549   Russell, A., & Khalili, N. (2006). A unified bounding surface plasticity model for

550   unsaturated soils. *International Journal for Numerical and Analytical Methods in*

551   *Geomechanics, 30*(3), 181-212.

552   Saada, A., Puccini, P., & Bianchini, G. (1989). Information package. In A. Saada & G.

553   Bianchini (Eds.), *Constitutive Equations for Granular Non-Cohesive Soils,* pp. 81-87.

554   Rotterdam: Balkema.

555   Sheng, D., Sloan, S., & Yu, H. (2000). Aspects of finite element implementation of critical

556   state models. *Computational mechanics, 26*(2), 185-196.

557   Sloan, S. W., Abbo, A. J., & Sheng, D. (2001). Refined explicit integration of elastoplastic

558   models with automatic error control. *Engineering Computations, 18*(1/2), 121-194.

559   Tatsuoka, F., & Ishihara, K. (1974). Drained deformation of sand under cyclic stresses

560   reversing direction. *Soils and Foundations, 14*(3), 51-65.

561   Verdugo, R., & Ishihara, K. (1996). The steady state of sandy soils. *Soils and Foundations,*

562   *36*(2), 81-91.

563

564

565   **Figure 1: Critical State Line (CSL) and Limiting Isotropic Compression Line (LICL)**

566

$N=2.0, R=2.0$

$N=2.0, R=6.0$

$N=3.0, R=2.0$

$N=3.0, R=6.0$
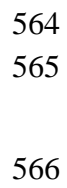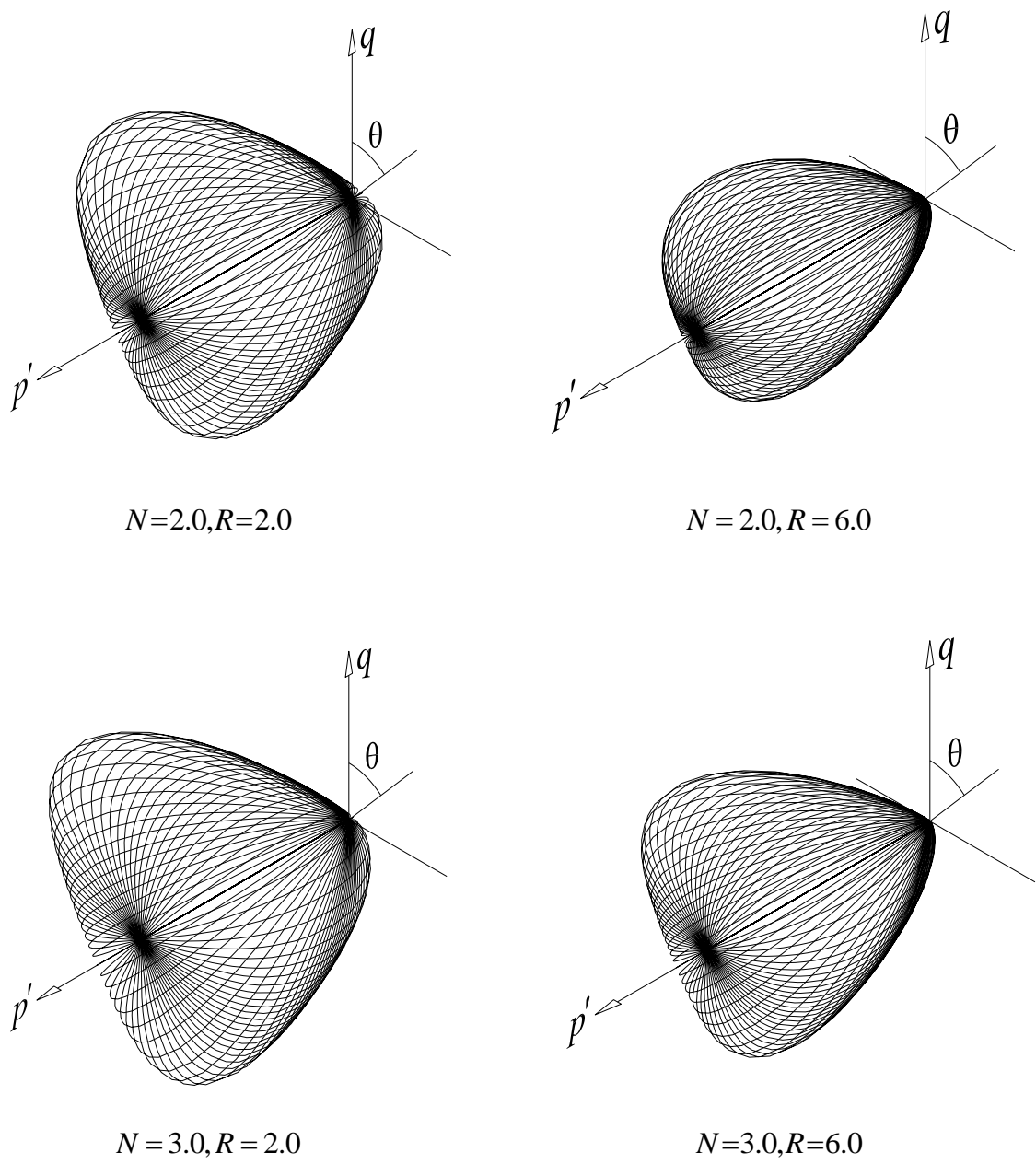
Figure 2: Effect of N and R on the shape of the bounding surface in $p'-q-\theta$

space

571
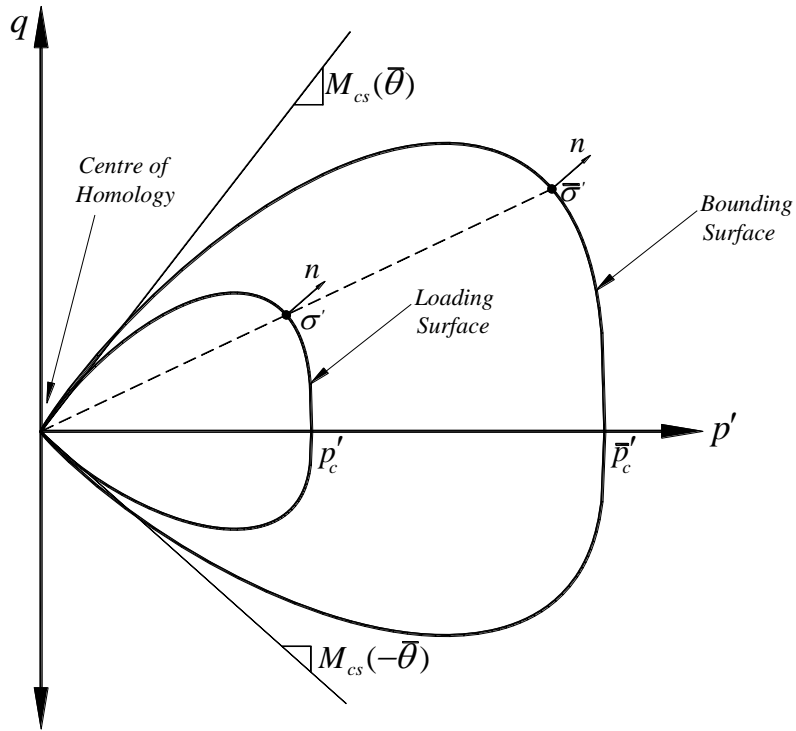
Figure 3: Loading surface and mapping rule for first time loading

573

574

Figure 4: Loading surface and mapping rule for unloading/reloading

(a) current study, (b) Khalili *et al.* (2005)

578
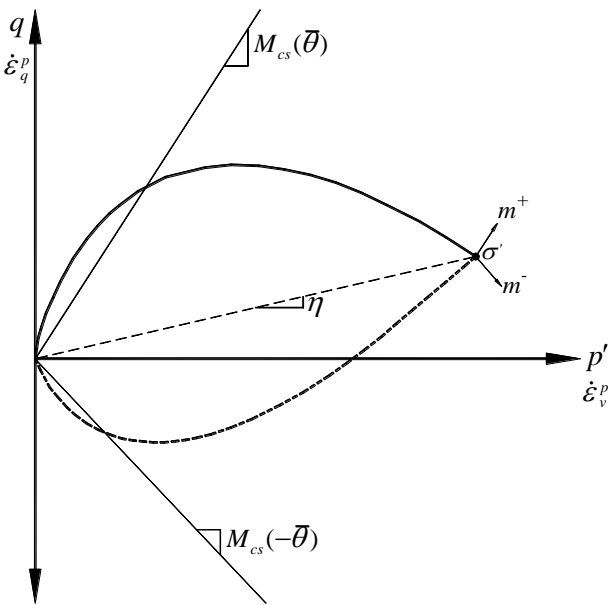
Figure 5: Vectors of plastic potential at σ' for compressive and extensive loading

579

580

581
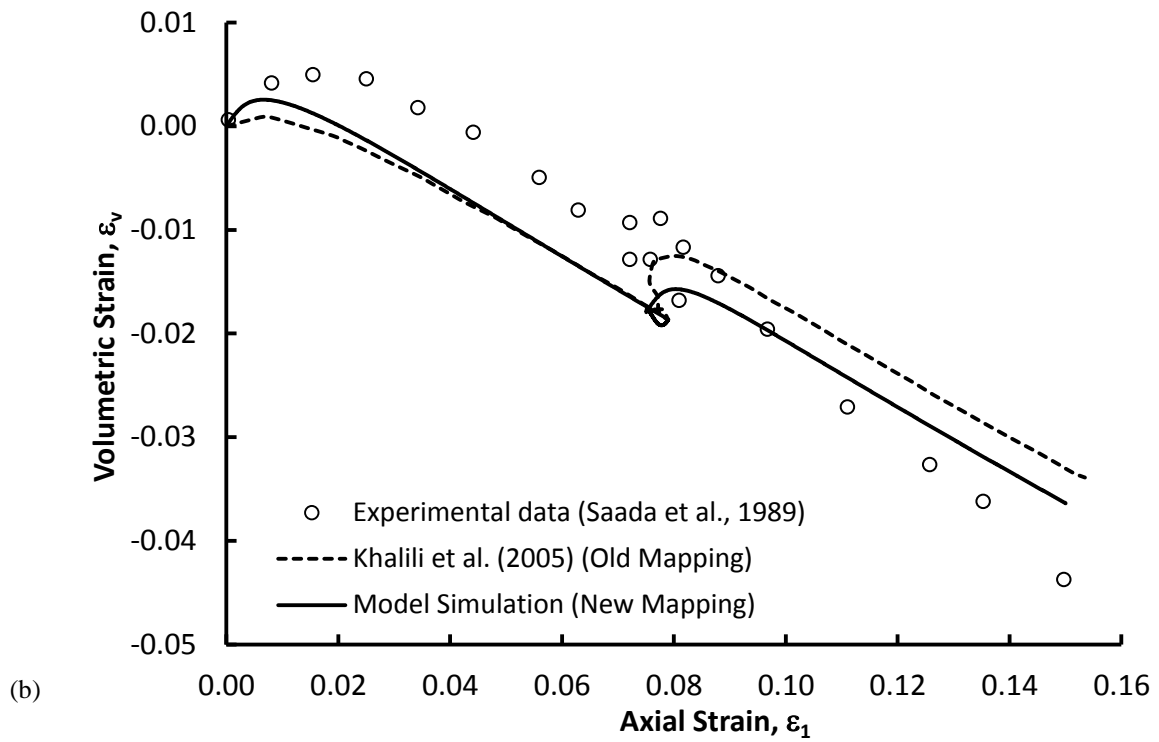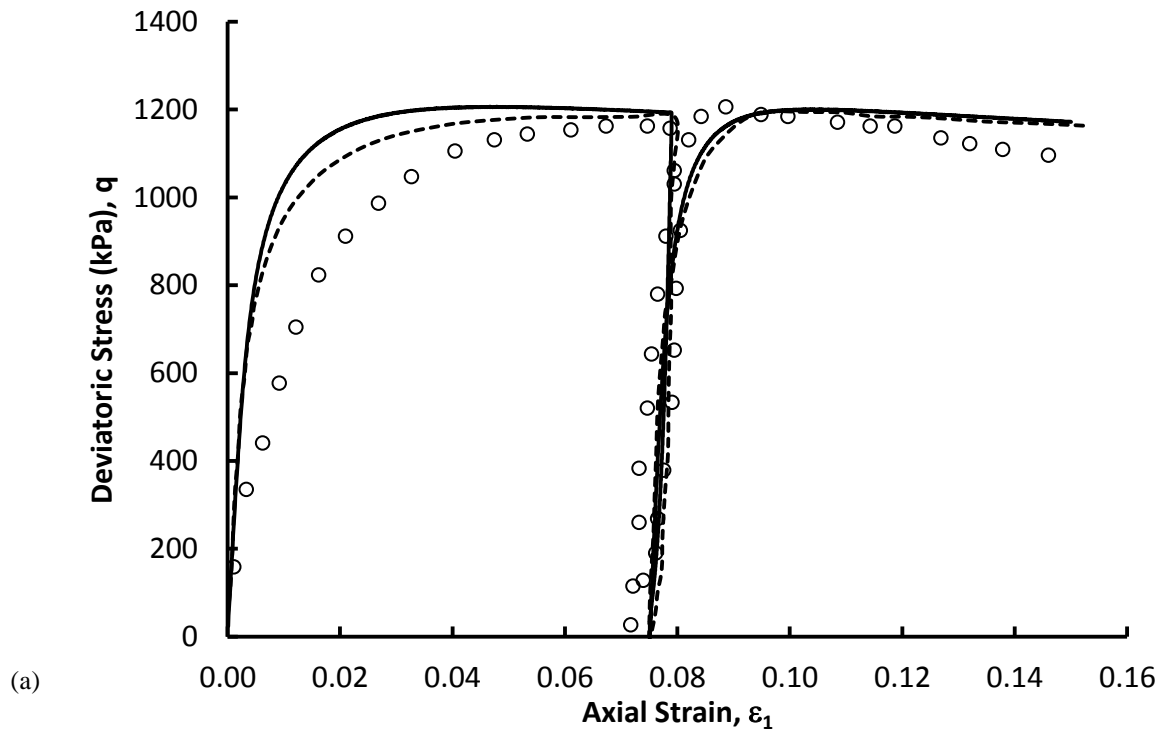
Figure 6: Drained cyclic test on a dense sample of Hostun sand

(a) $q - \varepsilon_1$ **plot and (b)** $\varepsilon_v - \varepsilon_1$ **plot**
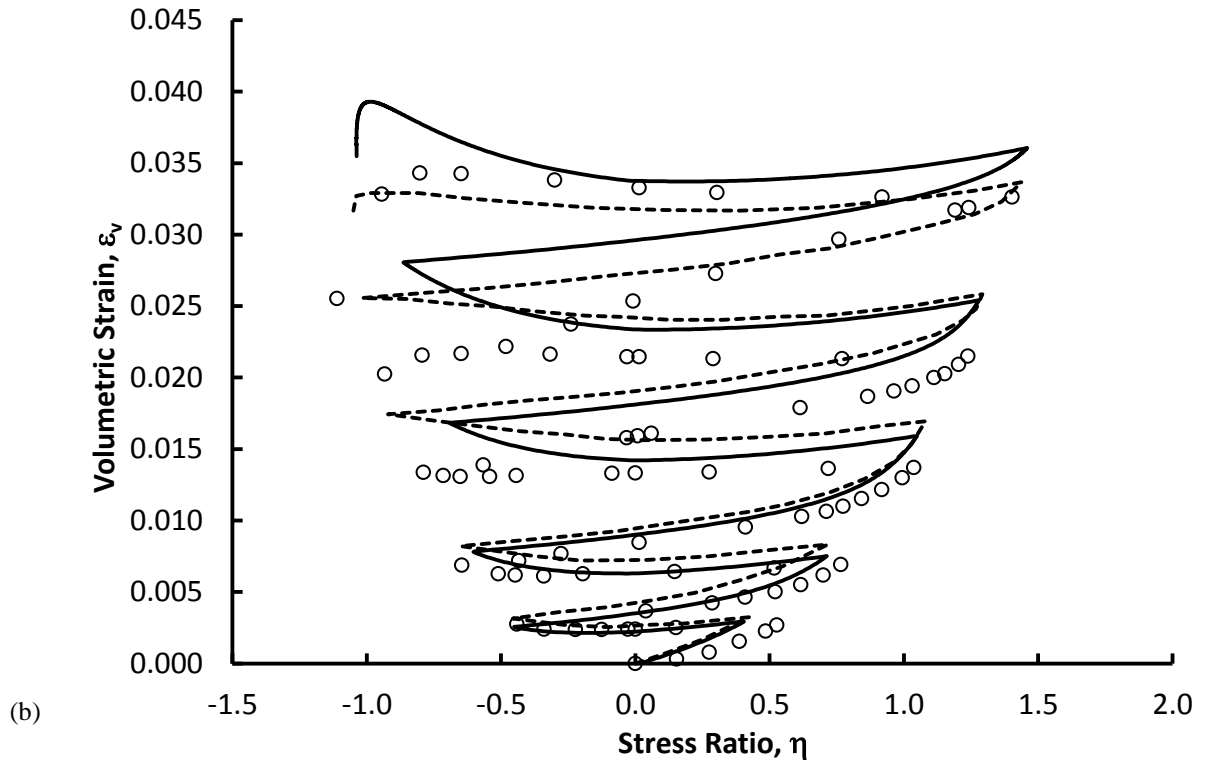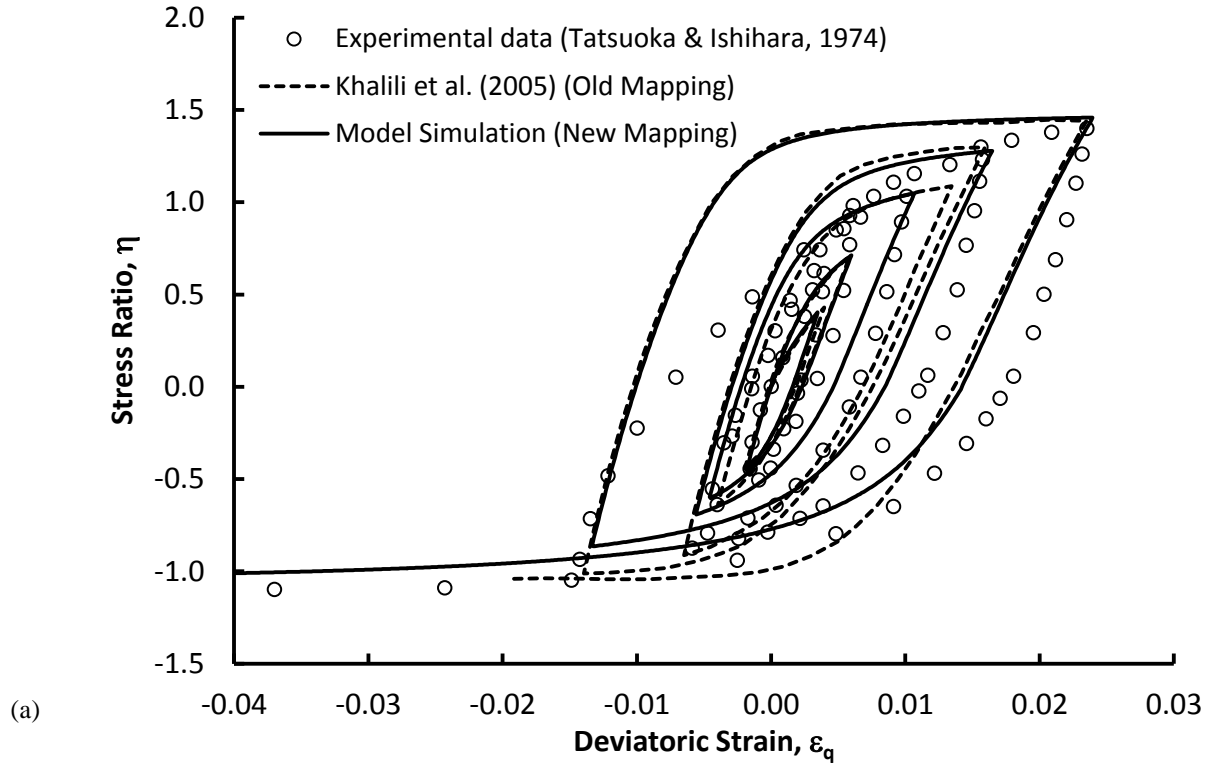
Figure 7: Drained cyclic test on a loose sample of Fuji River sand

(a) $\eta - \varepsilon_q$ plot and (b) $\varepsilon_v - \eta$ plot
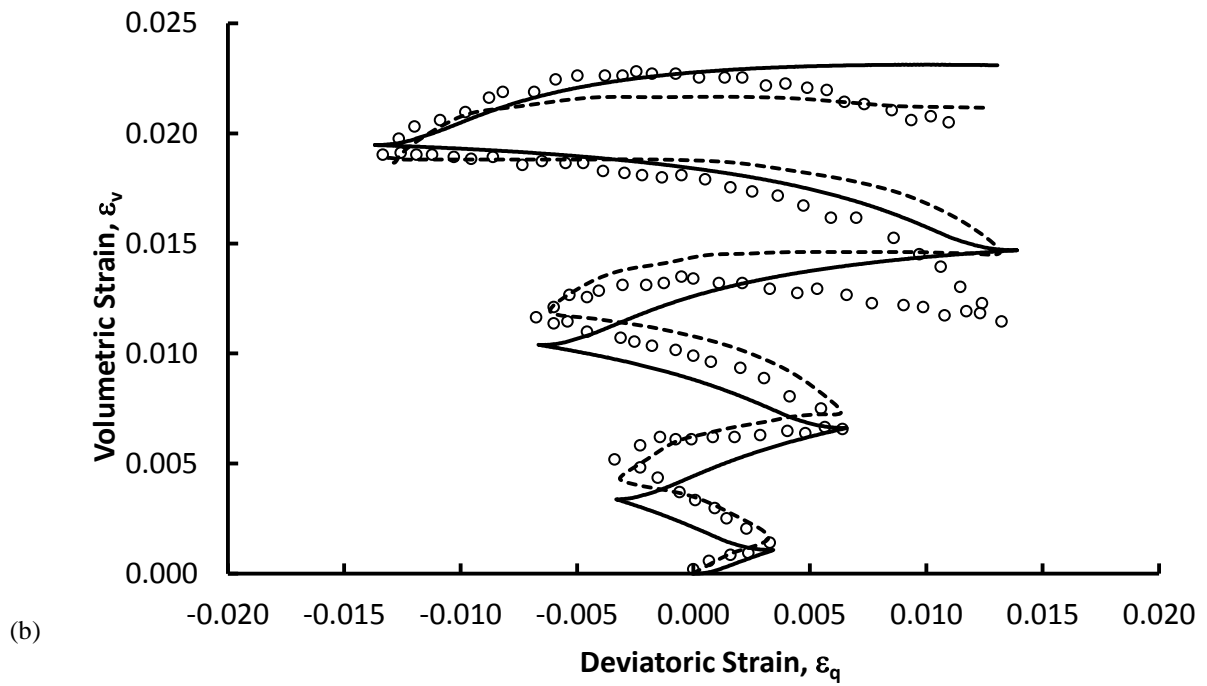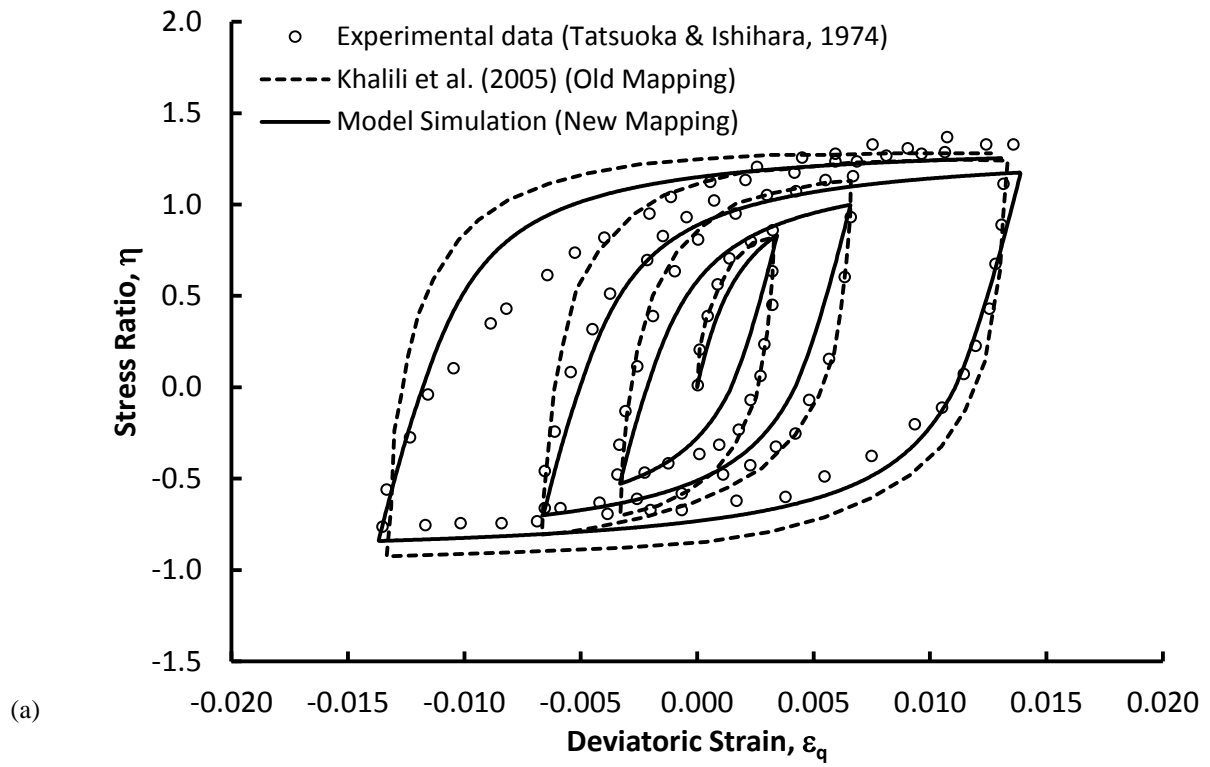
Figure 8: Drained cyclic test on a loose sample of Toyoura sand

(a) $\eta - \varepsilon_q$ **plot and (b)** $\varepsilon_v - \varepsilon_q$ **plot**

582

583

The figure shows a stress path diagram with axes q (vertical) and p' (horizontal). The Critical State Line is indicated with a dashed line. Points labeled O, O_1, O_2, A_1, A_2, C_1, C_2, C_3, C_4 are marked, with p'_0 below O_1 and p'_1 below O_2.

Test	Path
CIDC	$OO_1O_2C_1$
CIUC	$OO_1O_2C_2C_3$
CADC (p'=constant)	$OO_1A_1A_2C_1$
CADC (q=constant)	$OO_1A_1A_2C_4$
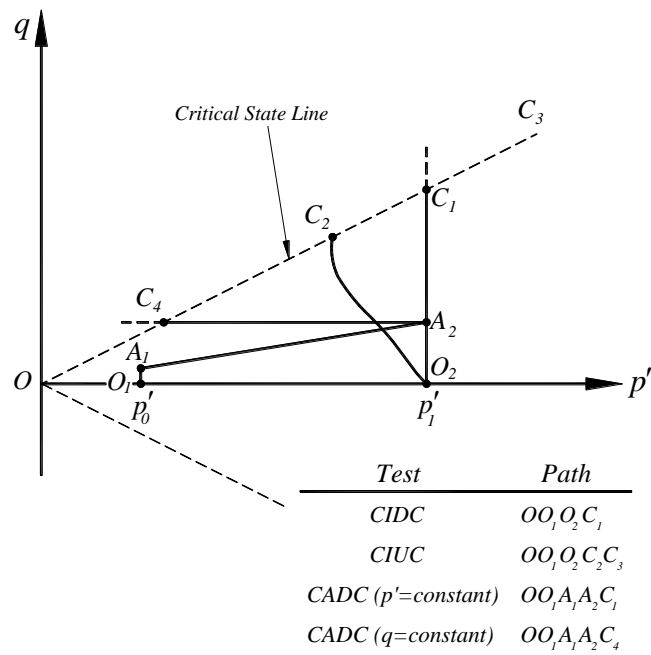
Figure 9: Stress paths in monotonic tests on Nevada Sand

(After Arulmoli *et al.*, 1992)
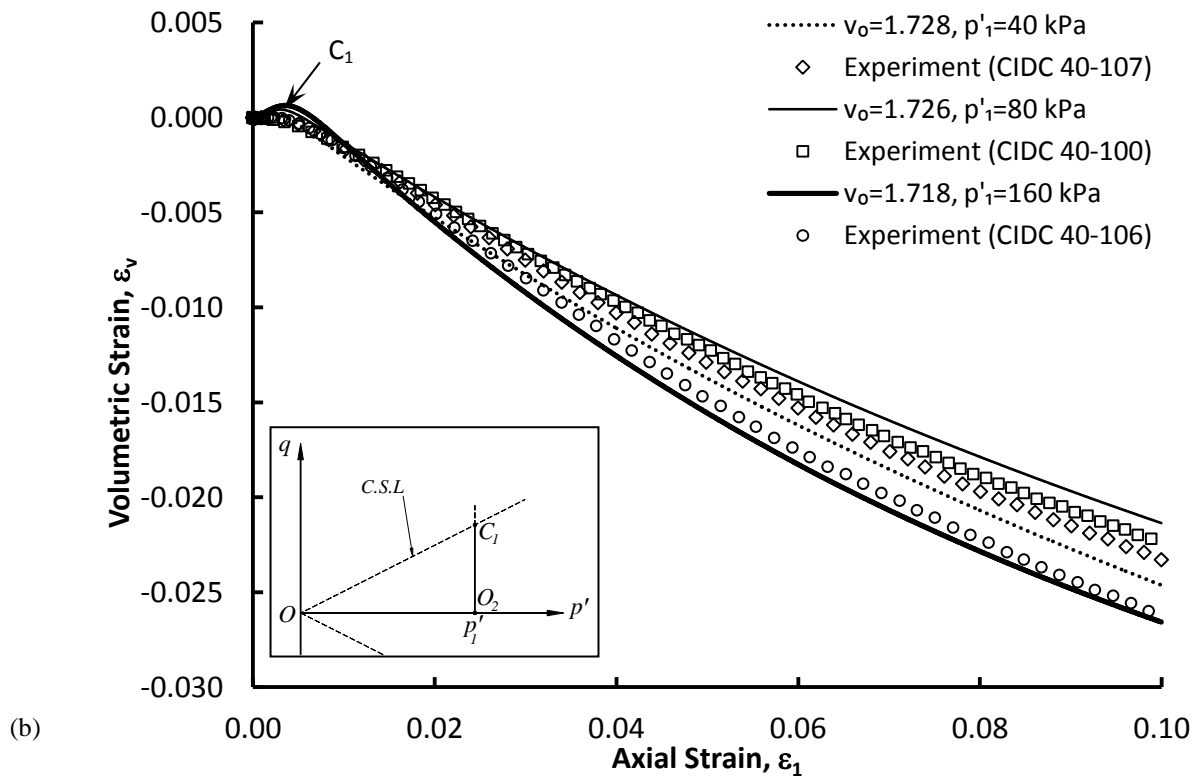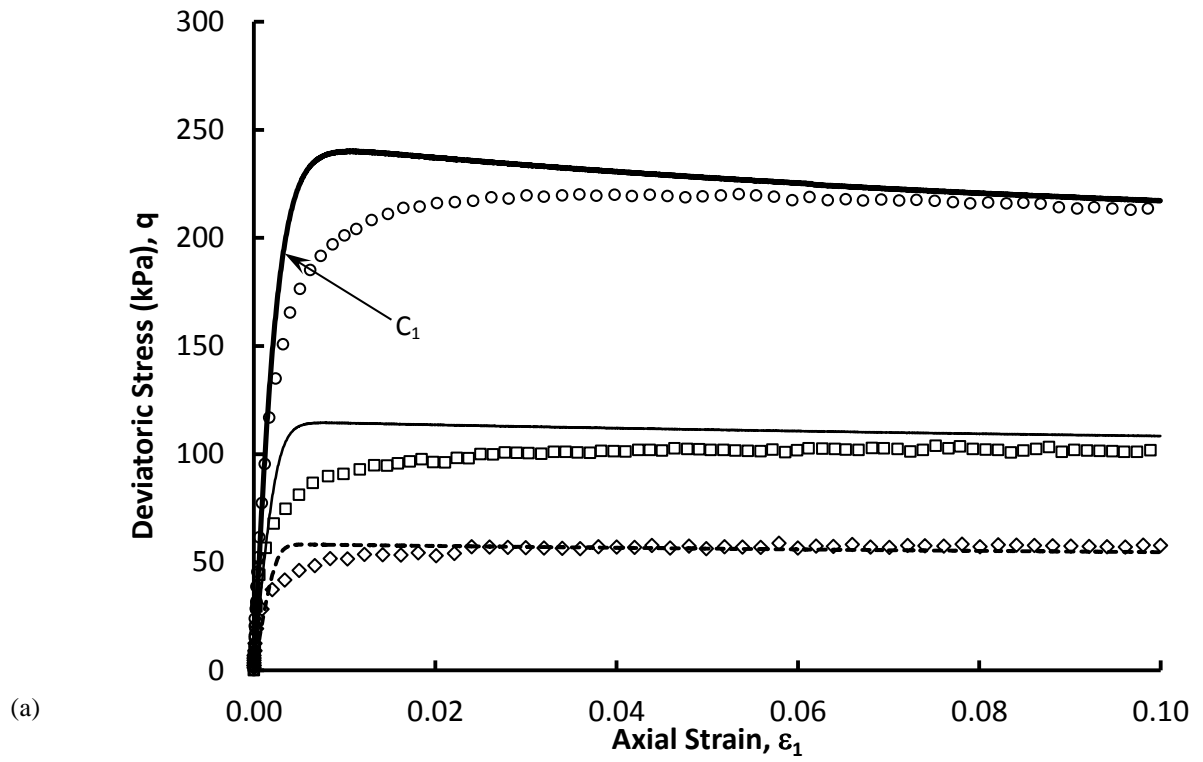
Figure 10: Drained CIDC tests on loose samples of Nevada sand $(D_r = 40\%)$

(a) $q - \varepsilon_1$ **plot and (b)** $\varepsilon_v - \varepsilon_1$ **plot**
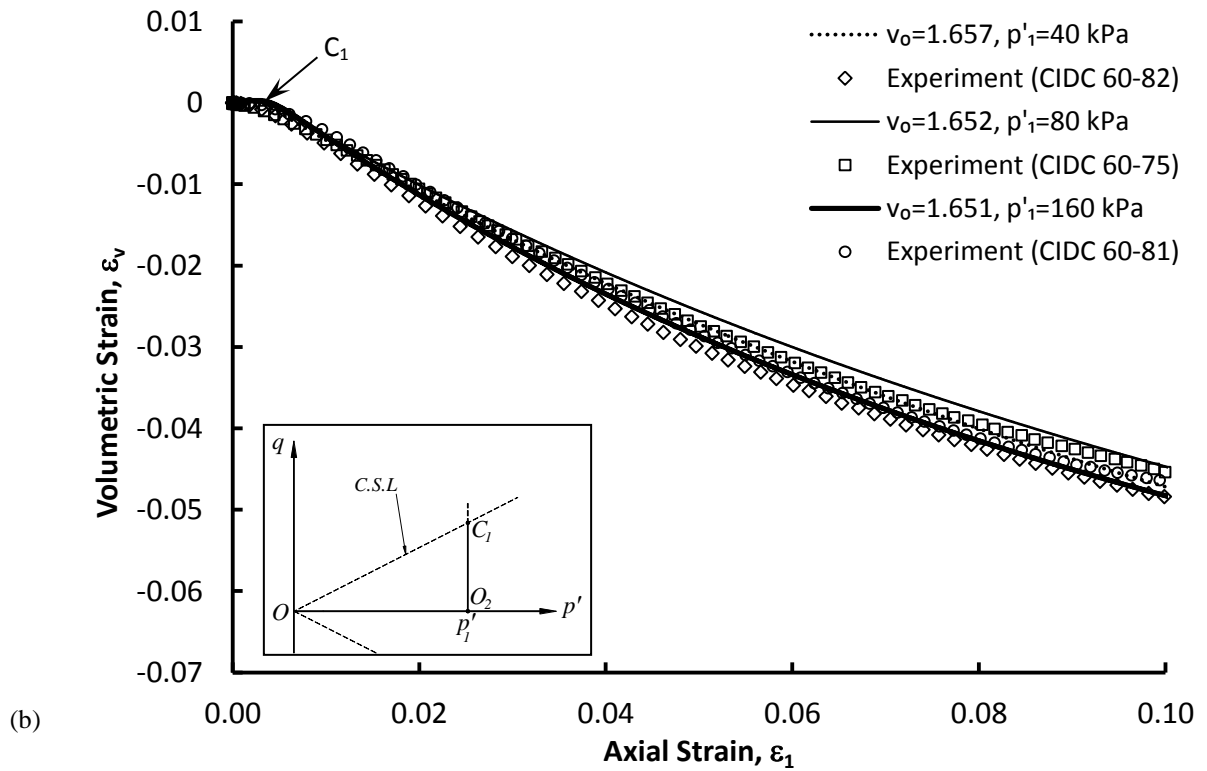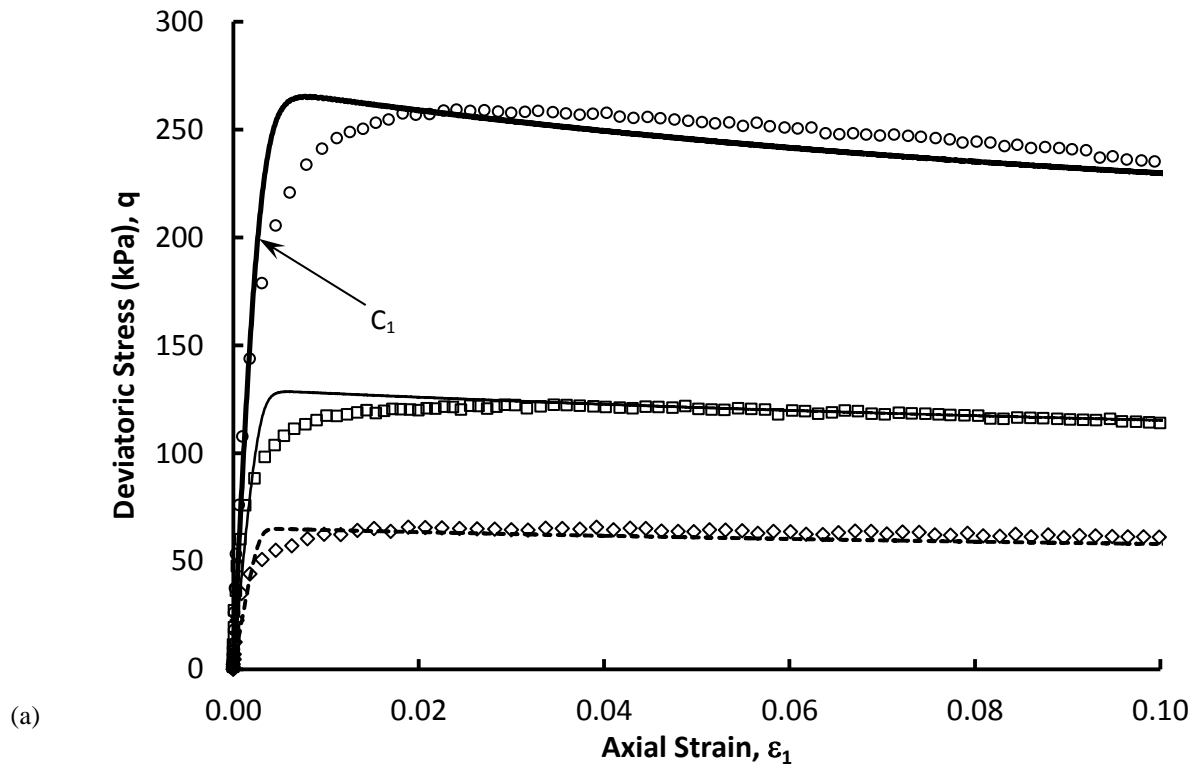
Figure 11: Drained CIDC tests on dense samples of Nevada sand $(D_r = 60\%)$

(a) $q - \varepsilon_1$ **plot and (b)** $\varepsilon_v - \varepsilon_1$ **plot**
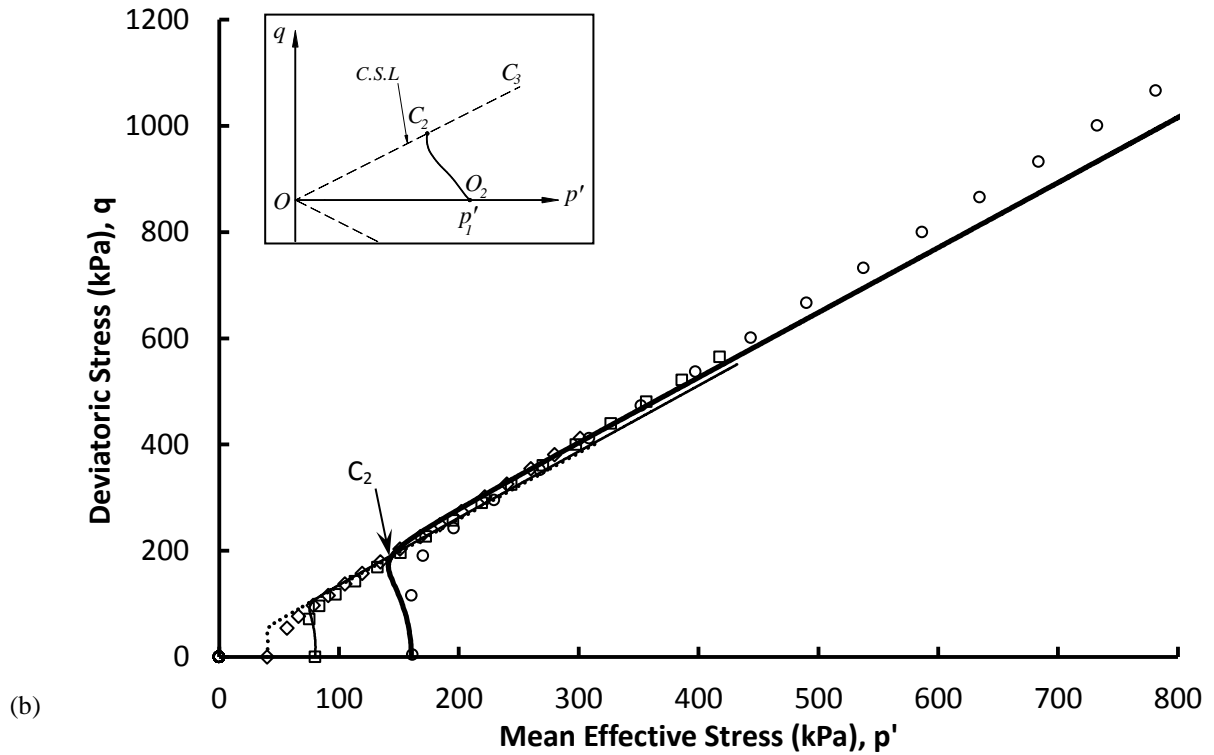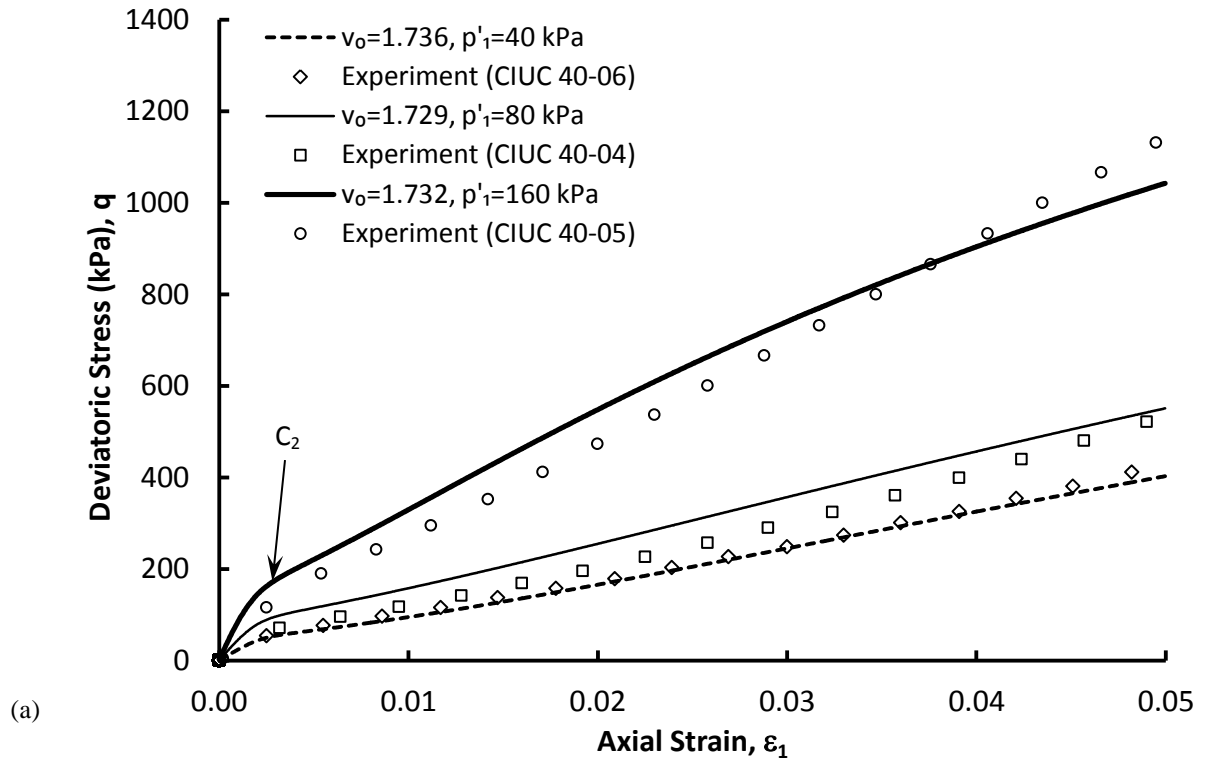
Figure 12: Undrained CIUC tests on loose samples of Nevada sand $(D_r = 40\%)$

(a) $q - \varepsilon_1$ **plot and (b)** $q - p'$ **plot**
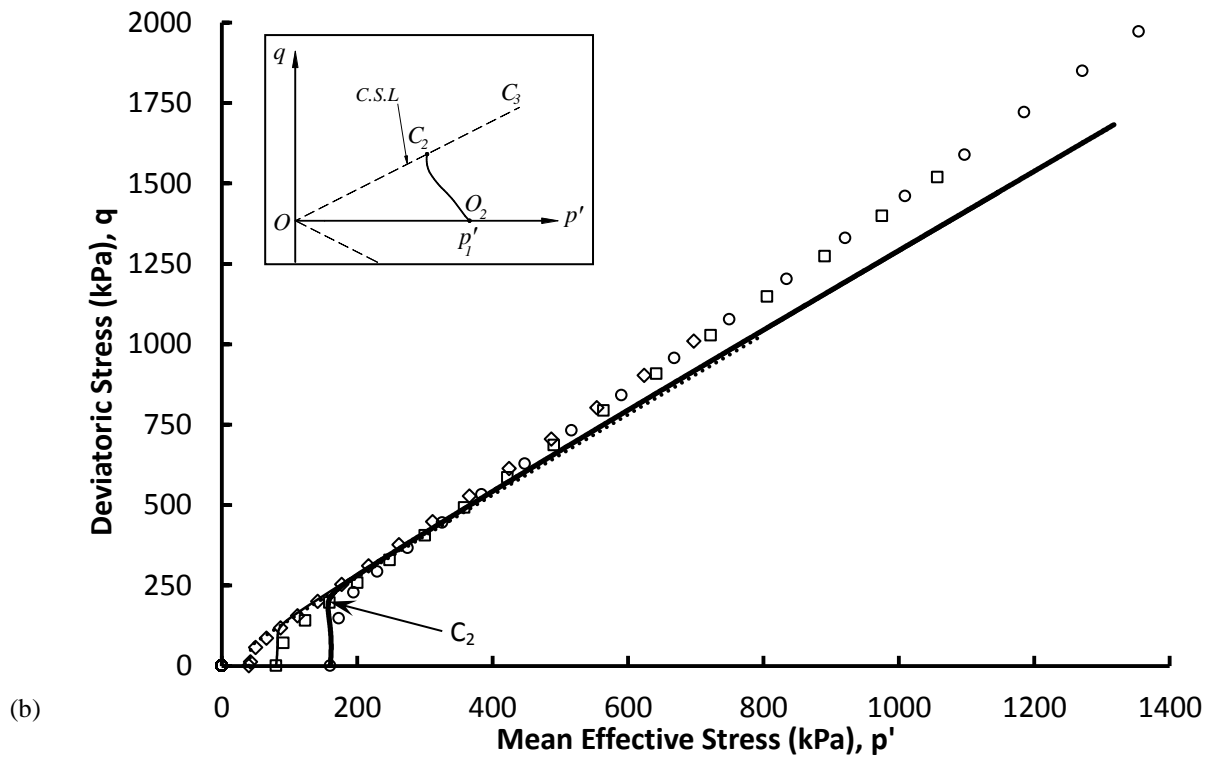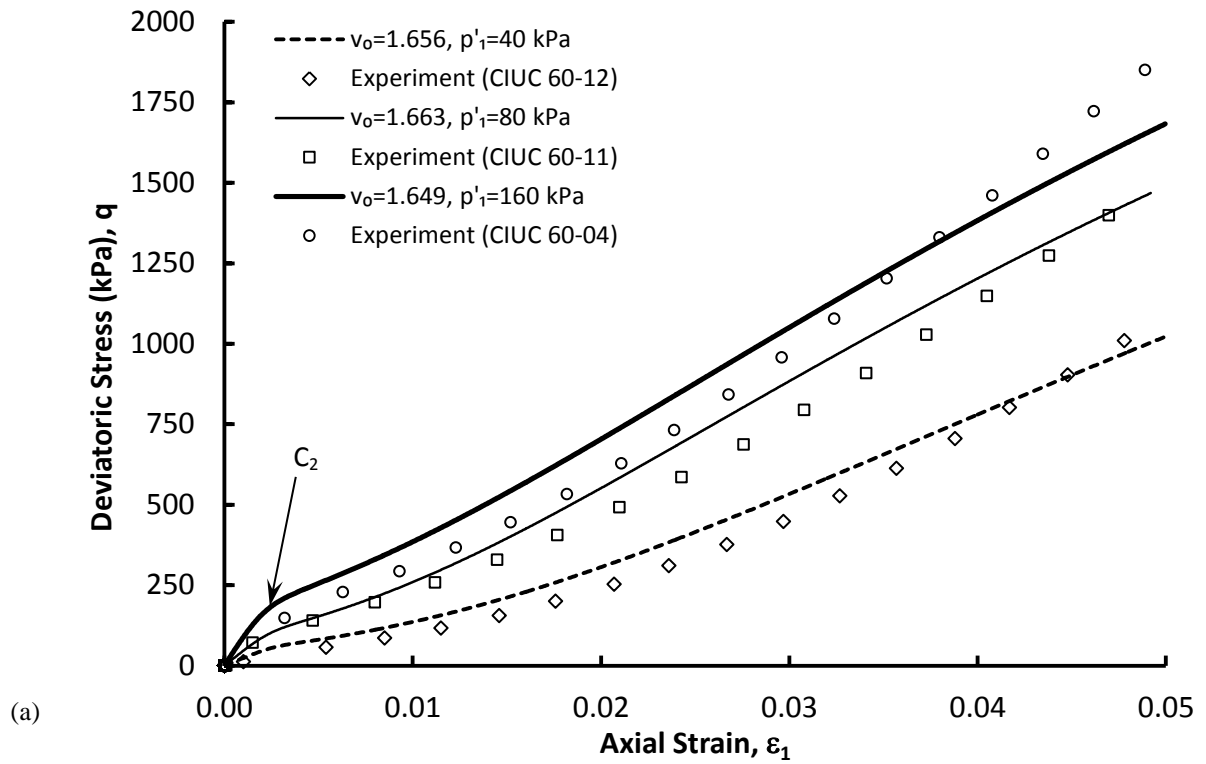
Figure 13: Undrained CIUC tests on dense samples of Nevada sand $(D_r = 60\%)$

(a) $q - \varepsilon_1$ **plot and (b)** $q - p'$ **plot**
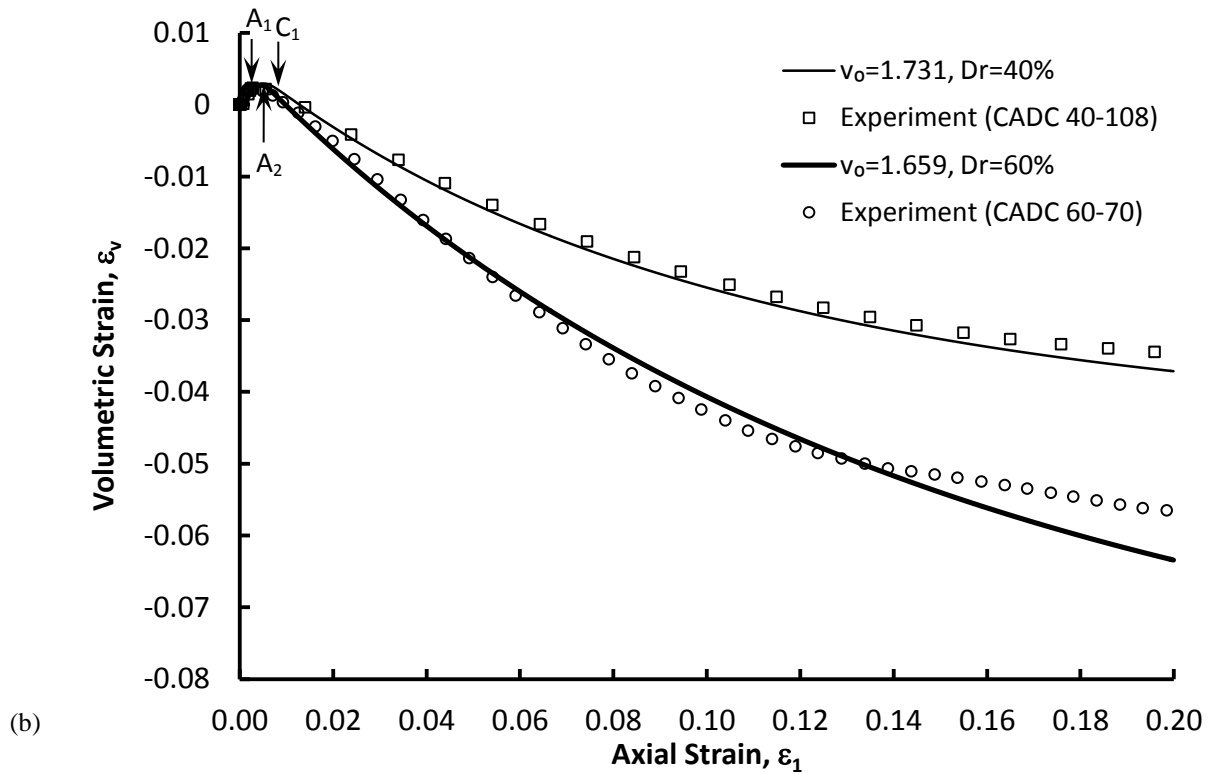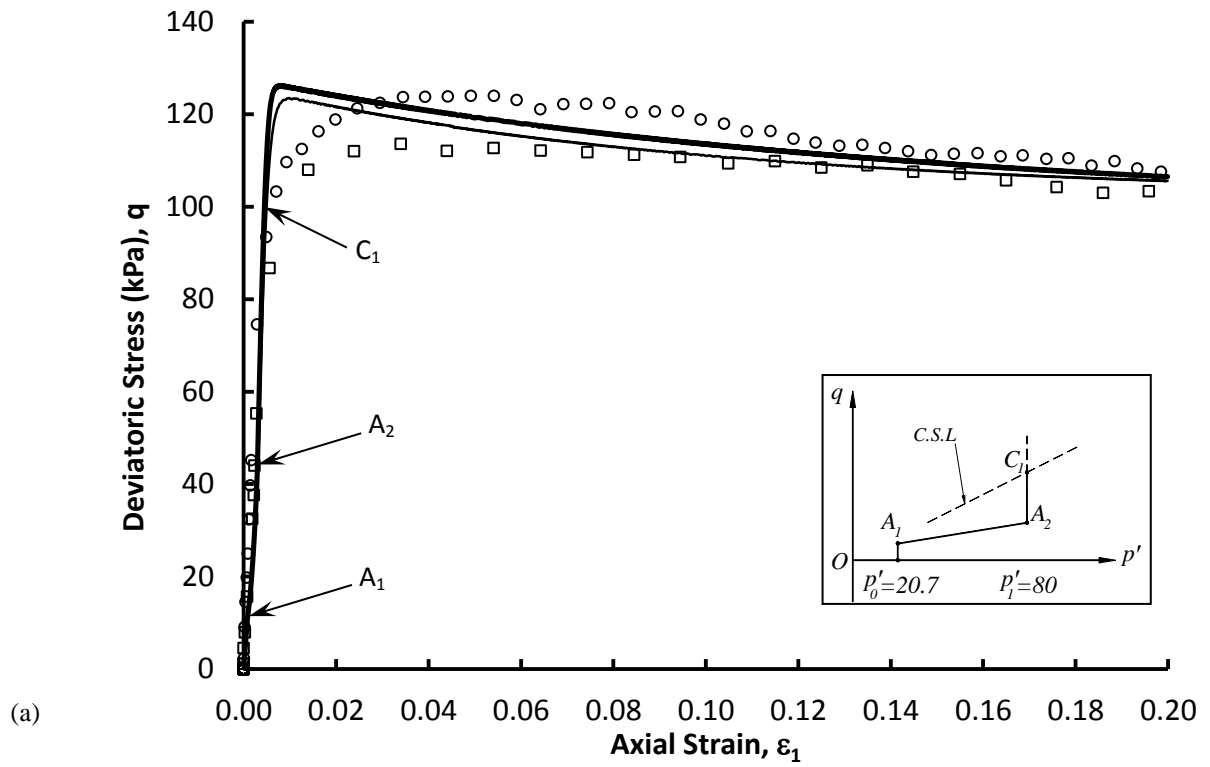
Figure 14: Drained CADC tests with constant p' on Nevada sand

(a) $q - \varepsilon_1$ **plot and (b)** $\varepsilon_v - \varepsilon_1$ **plot**
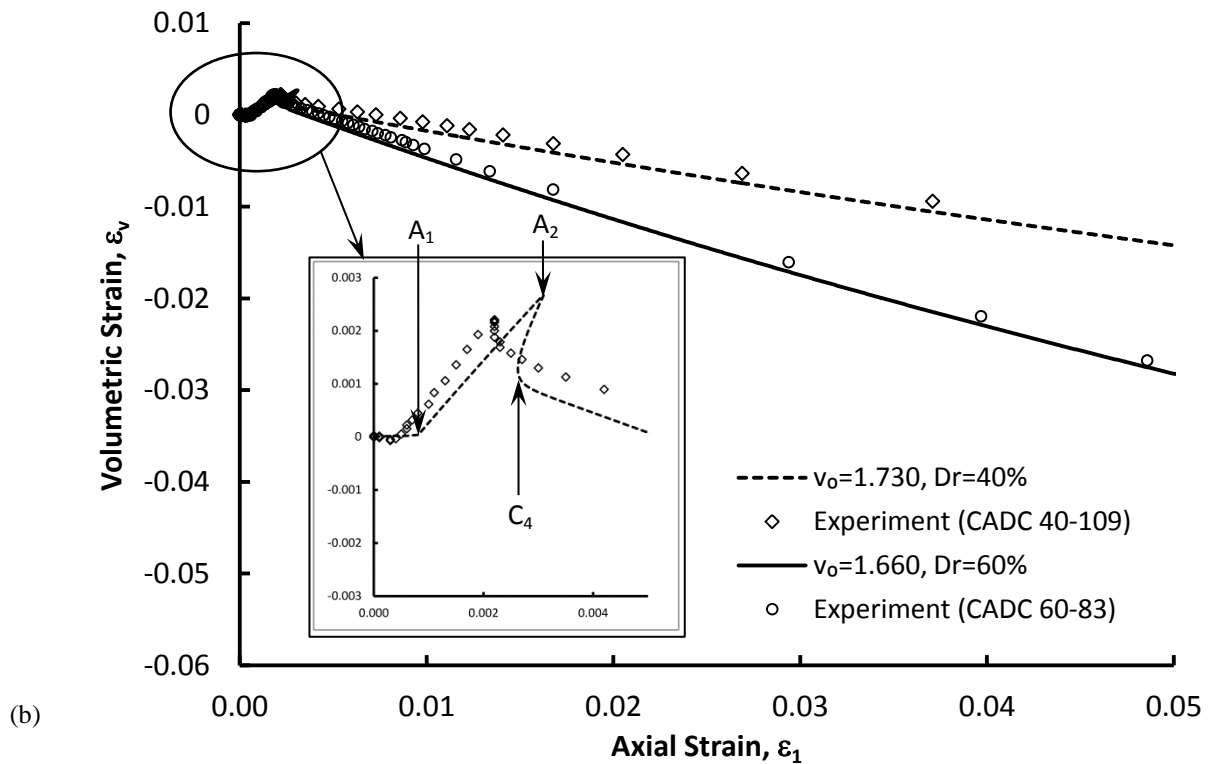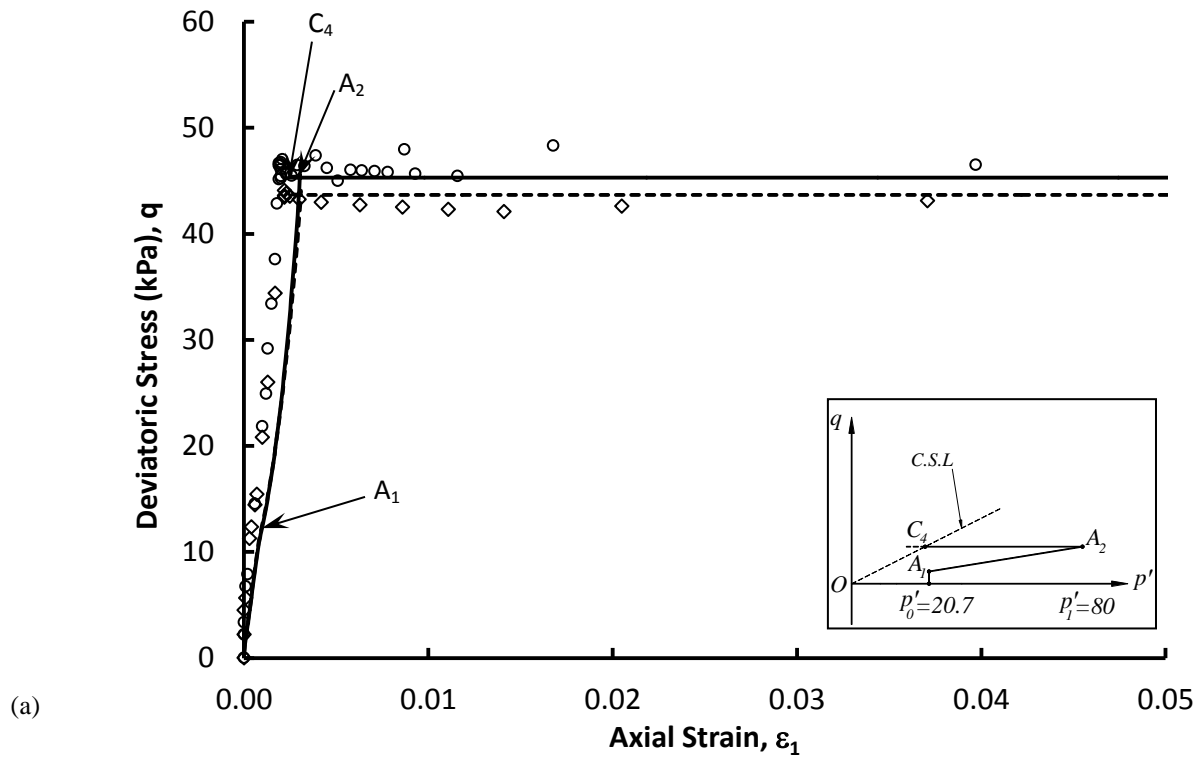
Figure 15: Drained CADC tests with constant q on Nevada sand

(a) $q - \varepsilon_1$ **plot and (b)** $\varepsilon_v - \varepsilon_1$ **plot**
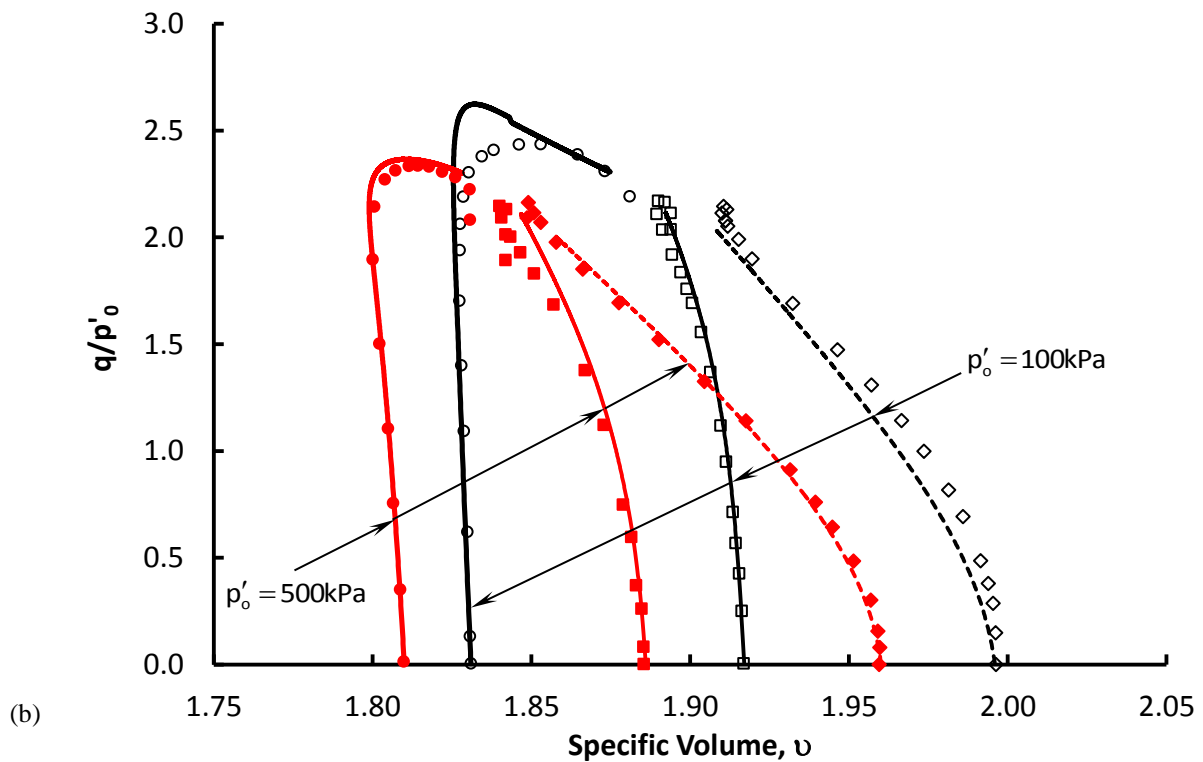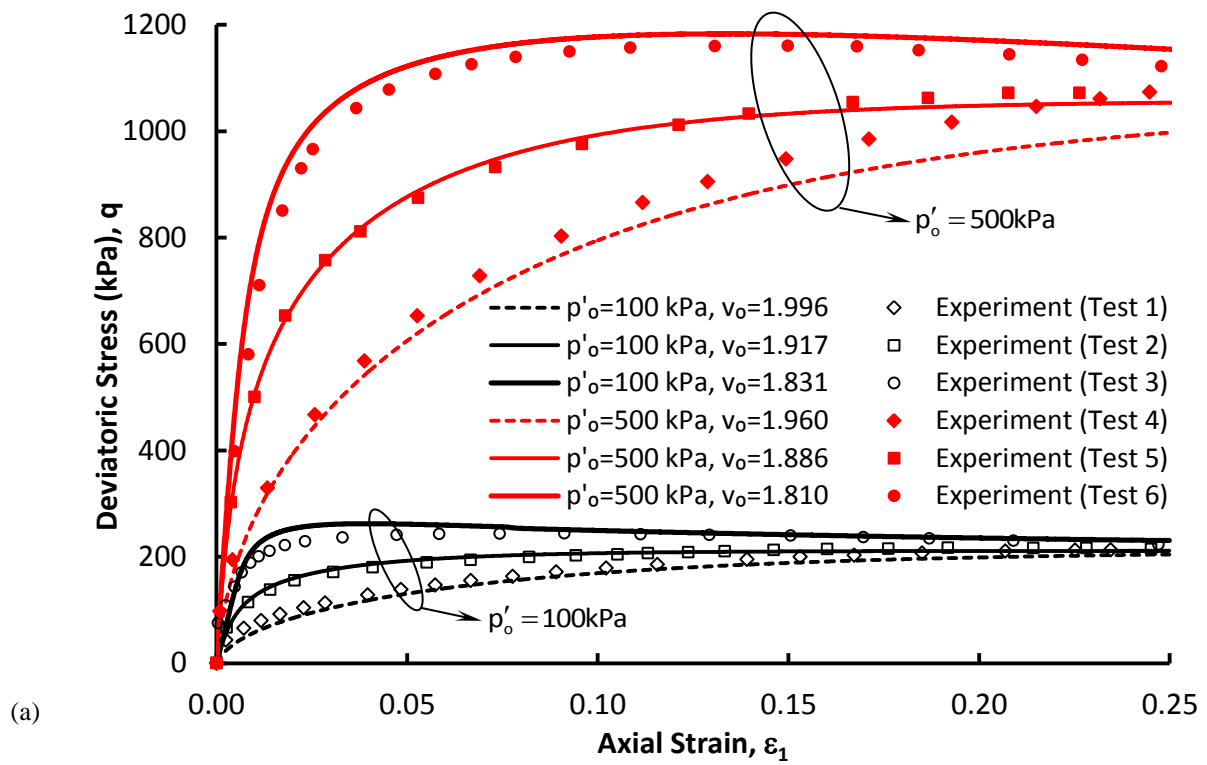
Figure 16: Drained tests on Toyoura sand

(a) $q - \varepsilon_1$ **plot and (b)** $q / p_0' - \upsilon$ **plot**

589
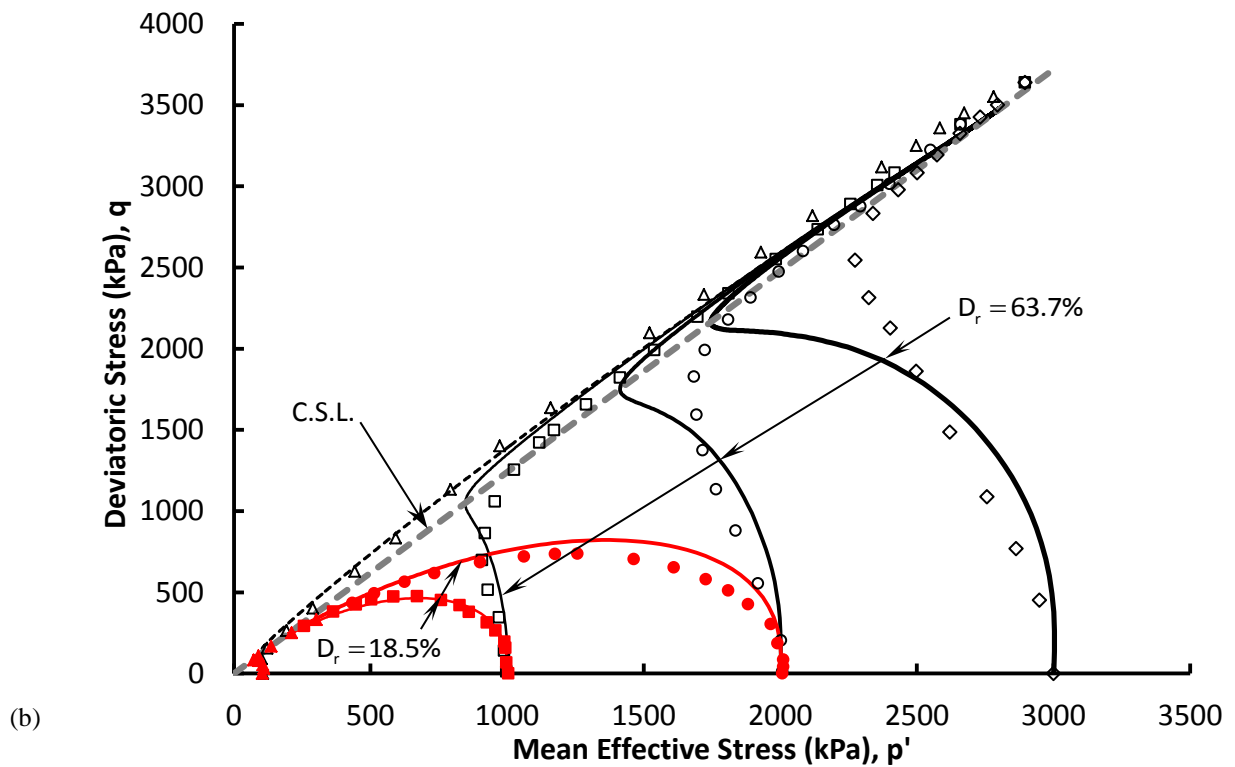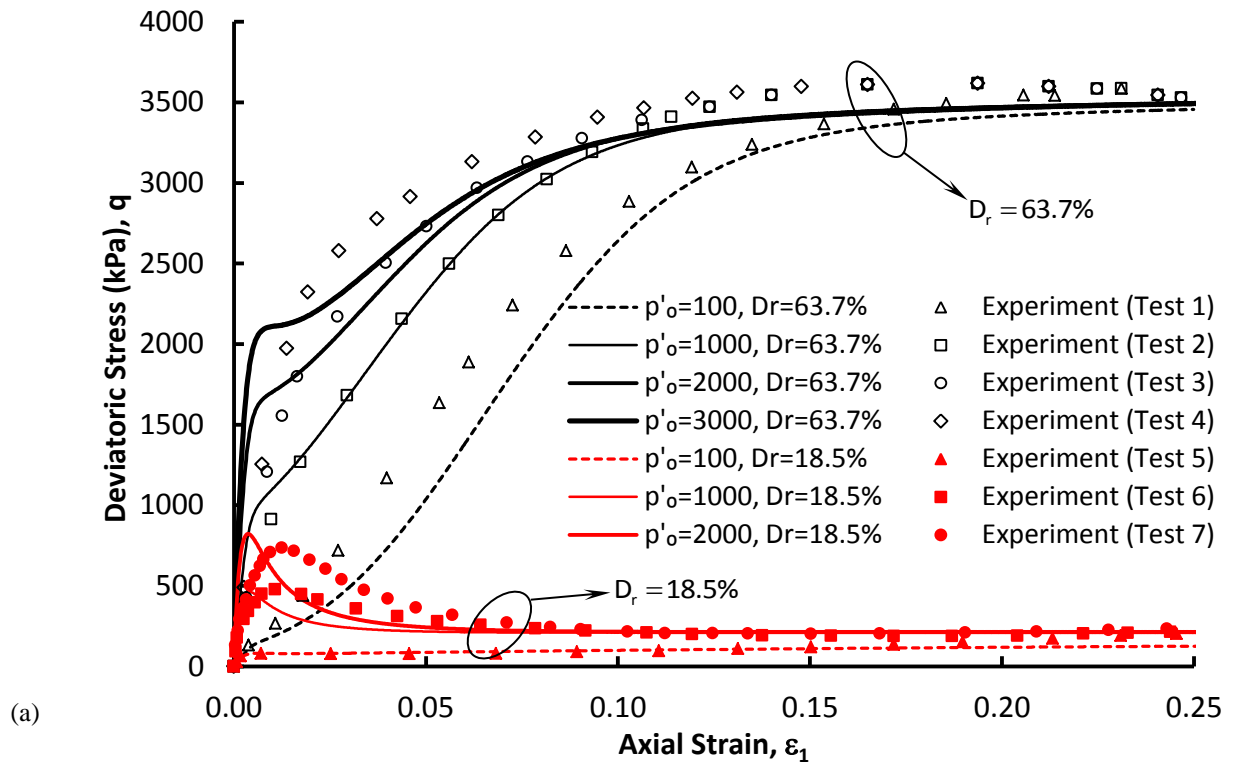
Figure 17: Undrained tests on Toyoura sand

(a) $q - \varepsilon_1$ **plot and (b)** $q - p'$ **plot**

590

591
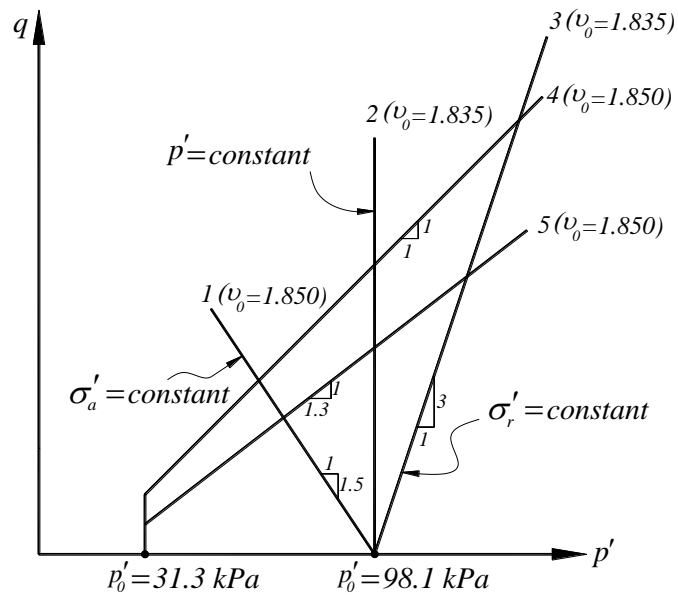
Figure 18: Stress paths used for tests on Toyoura sand (Pradhan *et al.*, 1989a)

592

593
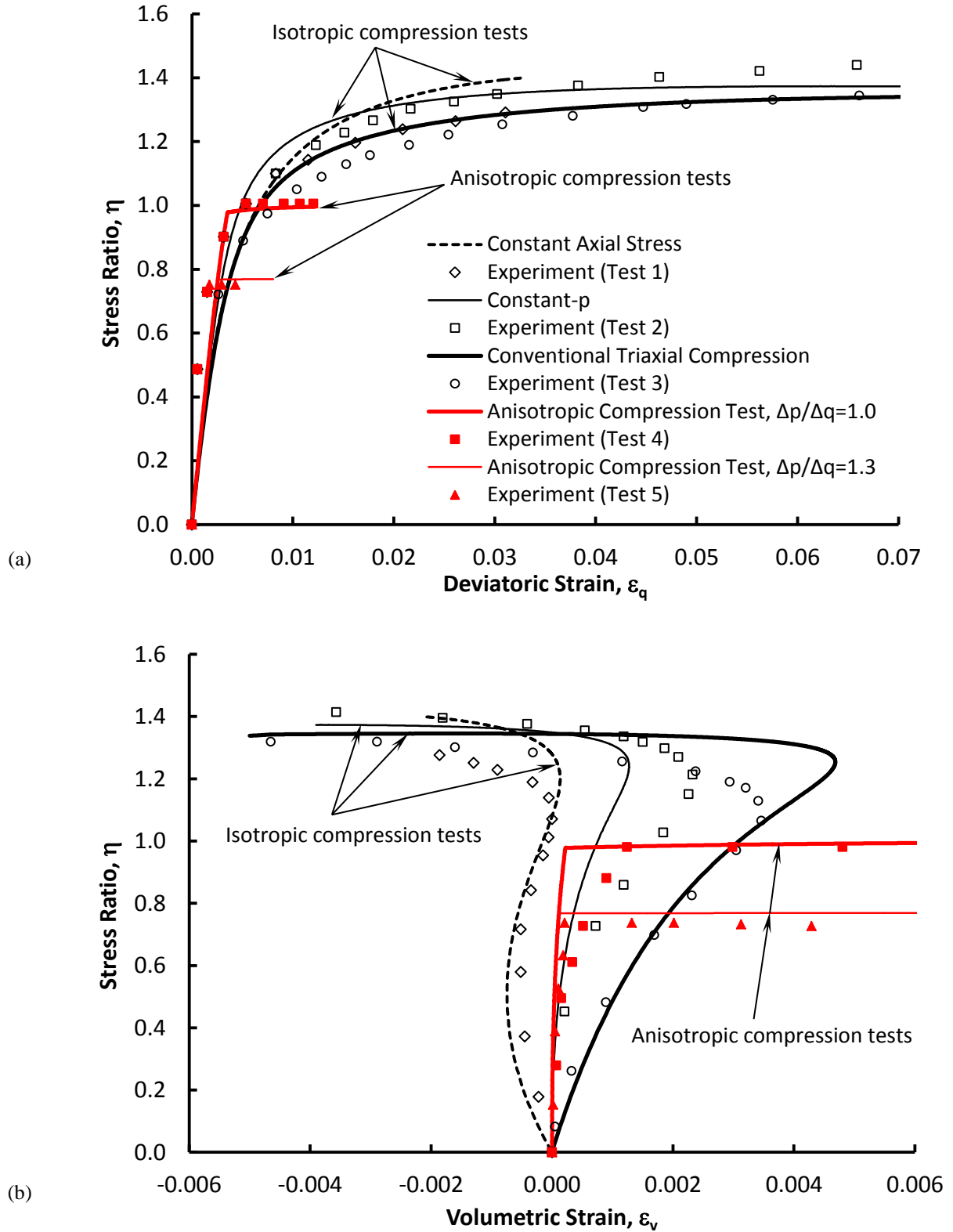
Figure 19: Drained tests with various stress paths on Toyoura sand

(a) $\eta - \varepsilon_q$ **plot and (b)** $\eta - \varepsilon_v$ **plot**
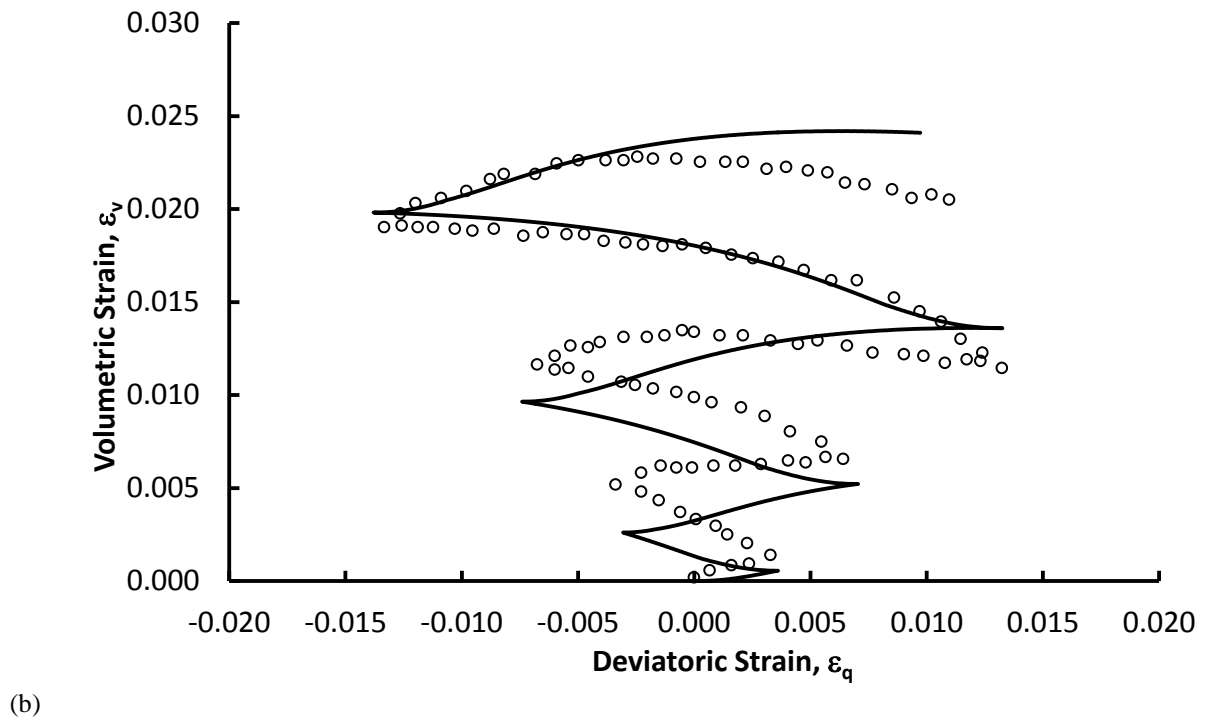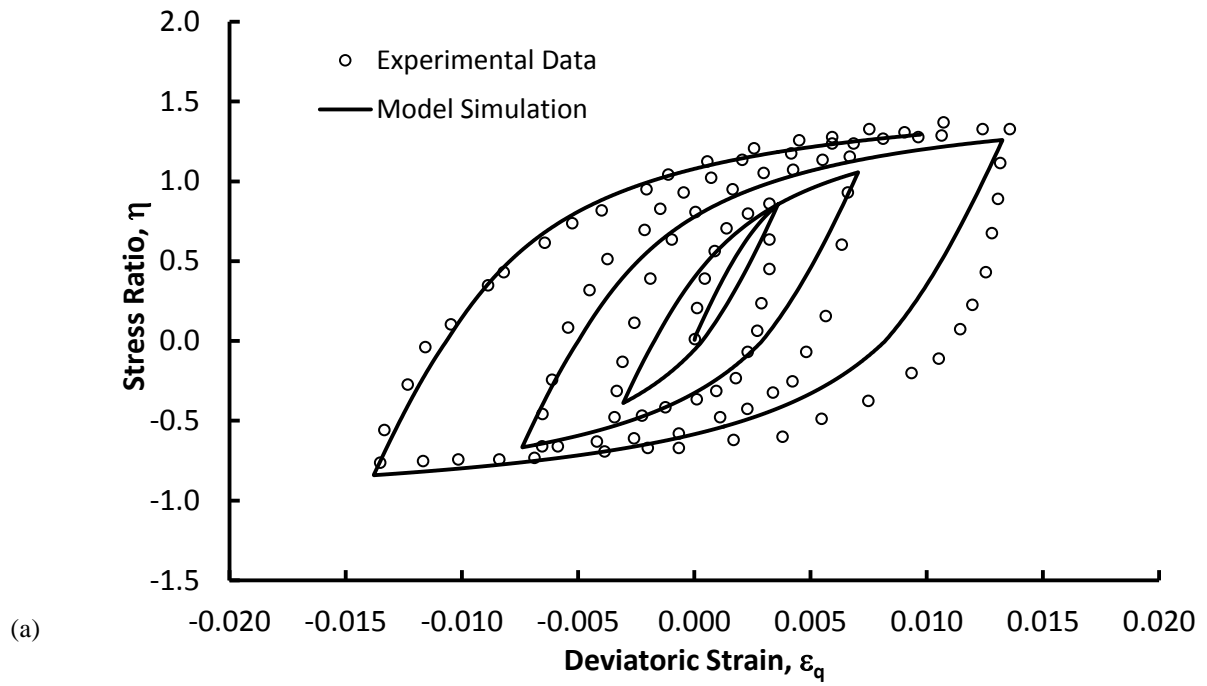
(a)

(b)

**Figure 20: Drained cyclic test on a loose sample of Toyoura sand
with increasing shear strain amplitude**

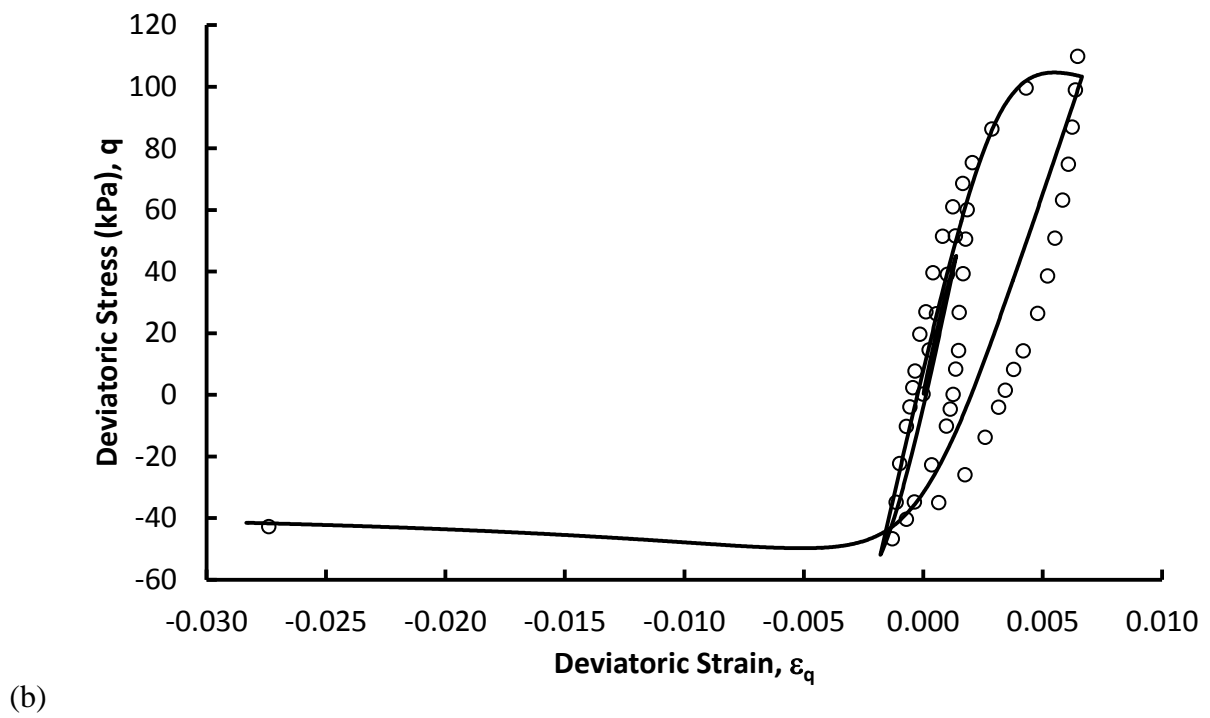**(a)** $\eta - \varepsilon_q$ **plot and (b)** $\varepsilon_v - \varepsilon_q$ **plot**
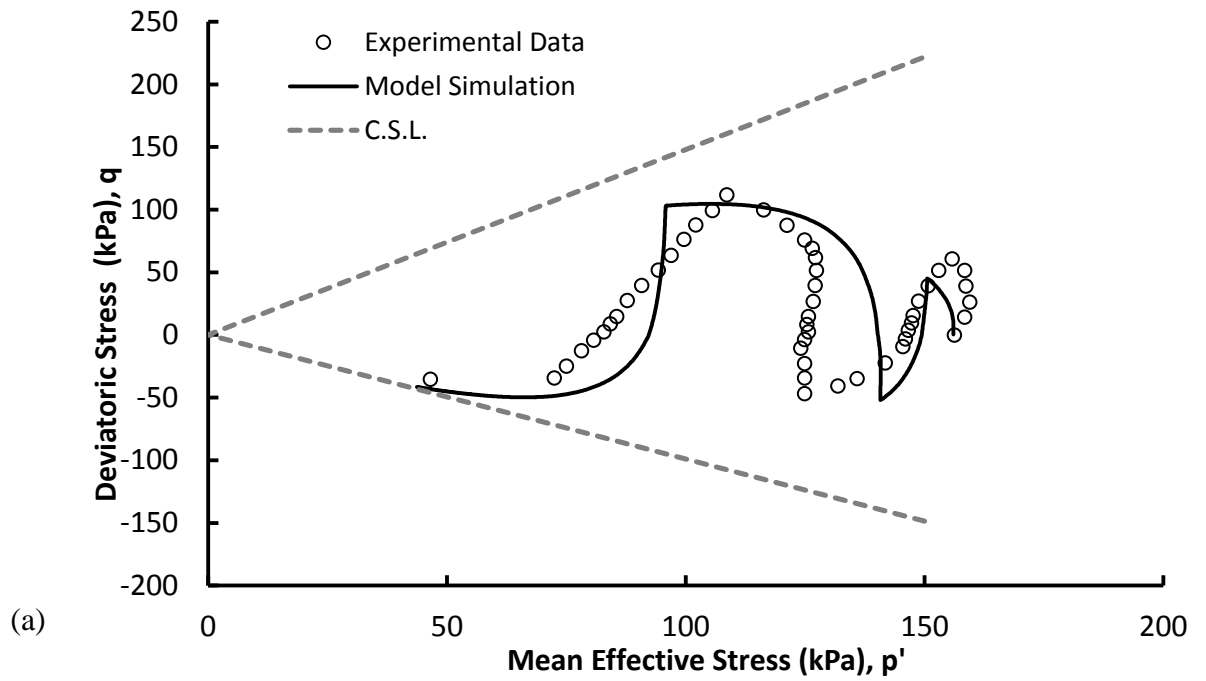
594

(a)

(b)

Figure 21: Drained cyclic test on a dense sample of Toyoura sand

with increasing shear strain amplitude

(a) $\eta - \varepsilon_q$ **plot and (b)** $\varepsilon_v - \eta$ **plot**

595

49

(a)

(b)
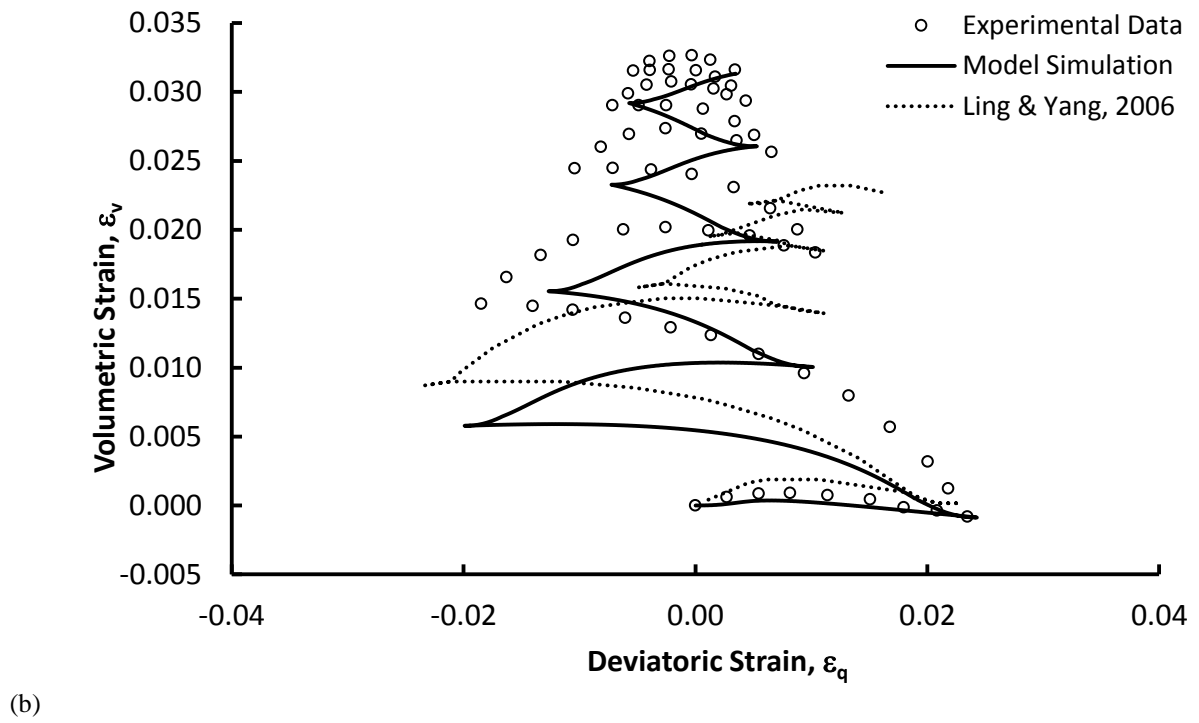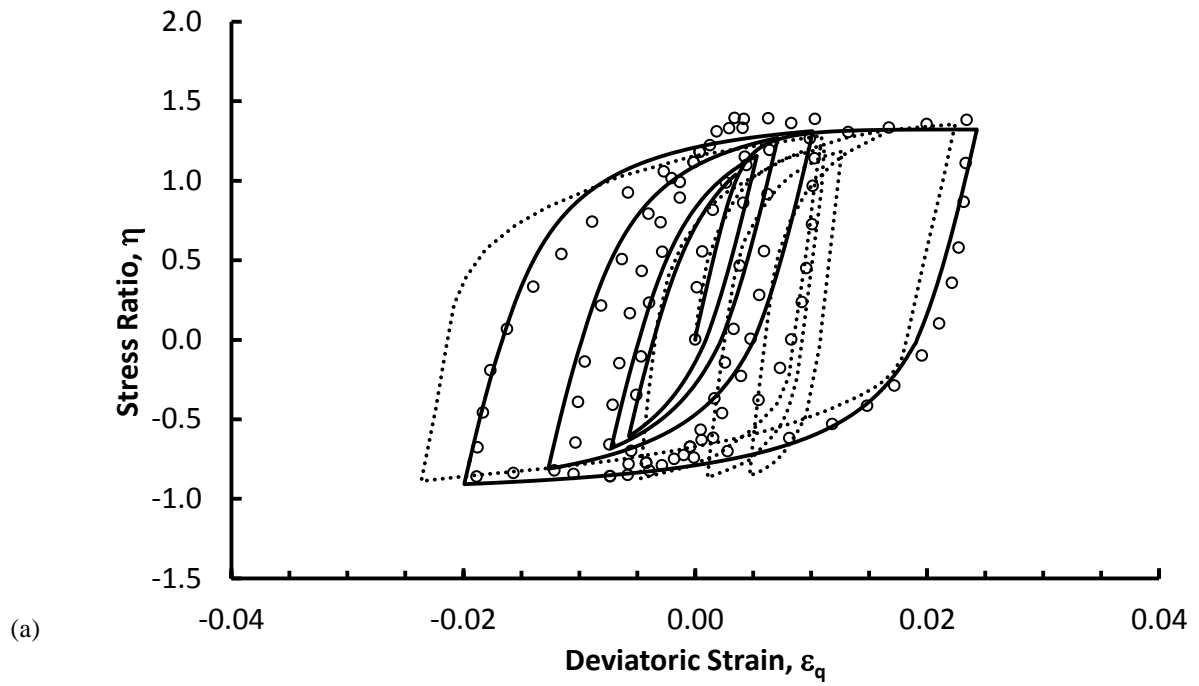
Figure 22: Drained cyclic test on a very loose sample of Toyoura sand

with decreasing shear strain amplitude

(a) $\eta - \varepsilon_q$ plot and (b) $\varepsilon_v - \varepsilon_q$ plot

596

(a)

(b)
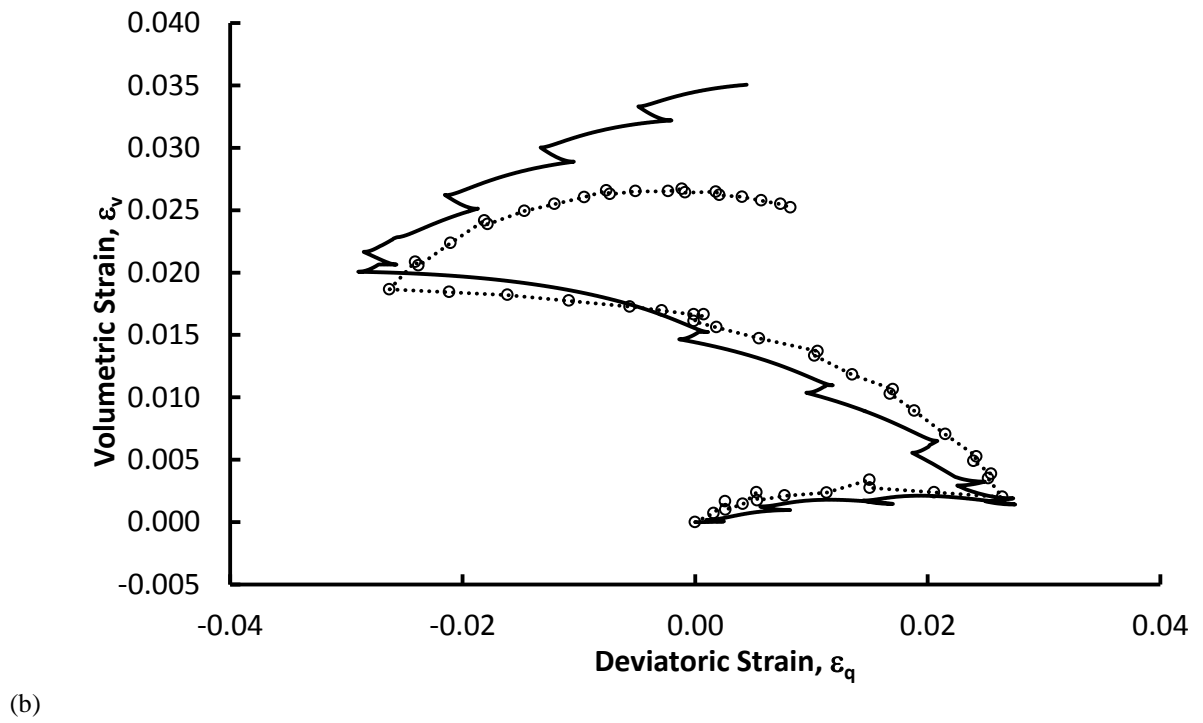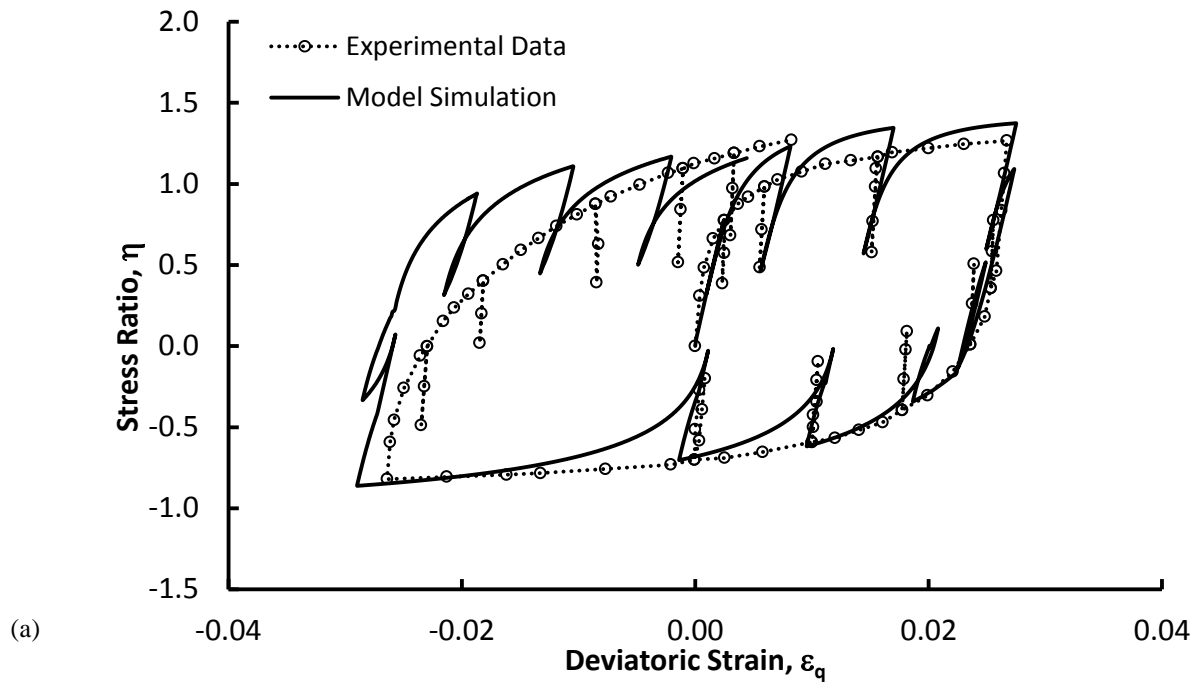
Figure 23: Drained cyclic test on a very loose sample of Toyoura sand

with small hysteresis loops

(a) $\eta - \varepsilon_q$ **plot and (b)** $\varepsilon_v - \varepsilon_q$ **plot**

597

(a)

(b)

Figure 24: Undrained cyclic test with constant cyclic amplitude

on a loose sample of Fuji River sand

(a) $q - p'$ **plot and (b)** $q - \varepsilon_q$ **plot**

598

(a)

(b)

Figure 25: Undrained cyclic test with irregular cyclic amplitude

on a loose sample of Fuji River sand

(a) $q - p'$ **plot and (b)** $q - \varepsilon_q$ **plot**

599

620   Figure 20: Drained cyclic test on a loose sample of Toyoura sand

621   Figure 21: Drained cyclic test on a dense sample of Toyoura sand

622   Figure 22: Drained cyclic test on a very loose sample of Toyoura sand

623   Figure 23: Drained cyclic test on a very loose sample of Toyoura sand

624   Figure 24: Undrained cyclic test with constant cyclic amplitude

625   Figure 25: Undrained cyclic test with irregular cyclic amplitude

626

627

Table 1: Material constants used in all simulations

Soil	Reference	κ	ν	M_{cs}	λ_0	λ_{cr}	p'_{cr} (kPa)	Γ_0	N	R	k	A
Nevada Sand	Arulmoli *et al.* (1992)	0.003	0.33	1.25	0.022	0.24	2000	1.910	1.5	3.0	2.0	1.5
Toyoura Sand	Verdugo and Ishihara (1996) & Pradhan *et al.* (1989a&b)	0.008	0.3	1.24	0.033	0.24	2000	2.075	2.5	8.5	2.0	1.0
Fuji River Sand	Ishihara *et al.* (1975)	0.01	0.3	1.48	0.032	0.21	1500	1.870	3.0	6.2	2.0	1.0

628

629

630 **Table 2: Values of k_m parameter used in different simulations**

Soil	k_{m0}		β_1	β_2
	First time loading	Unloading & reloading		
Nevada Sand	6.2	115.8	0.95	0.34
Toyoura Sand	1.2	76.0	1.05	0.3
Fuji River Sand	2.0	18.0	0	0

631

632

Table 2: Values of k_m parameter used in different simulations

633 **Table 3: State parameters used in simulation of cyclic tests**

Soil Type	Test Type	Sample/Load Condition	ID	υ_0	p_0' (kPa)
Toyoura Sand	Drained $p' = cst$	Loose	1	1.845	
		Dense	2	1.653	98.1
		Very Loose	3	1.865	
		Very Loose	4	1.855	
Fuji River Sand	Undrained cyclic	Constant Amplitude	1	1.735	212.6
		Irregular Amplitude	2	1.749	156.0

634

635

636